BAMS Article

The 2019 Southern Hemisphere Stratospheric Polar Vortex Weakening and Its Impacts

Eun-Pa Lim, Harry H. Hendon, Amy H. Butler, David W. J. Thompson, Zachary D. Lawrence, Adam A. Scaife, Theodore G. Shepherd, Inna Polichtchouk, Hisashi Nakamura, Chiaki Kobayashi, Ruth Comer, Lawrence Coy, Andrew Dowdy, Rene D. Garreaud, Paul A. Newman, and Guomin Wang

ABSTRACT: This study offers an overview of the low-frequency (i.e., monthly to seasonal) evolution, dynamics, predictability, and surface impacts of a rare Southern Hemisphere (SH) stratospheric warming that occurred in austral spring 2019. Between late August and mid-September 2019, the stratospheric circumpolar westerly jet weakened rapidly, and Antarctic stratospheric temperatures rose dramatically. The deceleration of the vortex at 10 hPa was as drastic as that of the first-ever-observed major sudden stratospheric warming in the SH during 2002, while the mean Antarctic warming over the course of spring 2019 broke the previous record of 2002 by ~50% in the midstratosphere. This event was preceded by a poleward shift of the SH polar night jet in the uppermost stratosphere in early winter, which was then followed by record-strong planetary wave-1 activity propagating upward from the troposphere in August that acted to dramatically weaken the polar vortex throughout the depth of the stratosphere. The weakened vortex winds and elevated temperatures moved downward to the surface from mid-October to December, promoting a record strong swing of the southern annular mode (SAM) to its negative phase. This record-negative SAM appeared to be a primary driver of the extreme hot and dry conditions over subtropical eastern Australia that accompanied the severe wildfires that occurred in late spring 2019. State-of-the-art dynamical seasonal forecast systems skillfully predicted the significant vortex weakening of spring 2019 and subsequent development of negative SAM from as early as late July.

KEYWORDS: Antarctic Oscillation; Planetary waves; Stratospheric circulation; Extreme events; Stratosphere-troposphere coupling; Climate prediction

https://doi.org/10.1175/BAMS-D-20-0112.1
Corresponding author: Eun-Pa Lim, eun-pa.lim@bom.gov.au
Supplemental material: https://doi.org/10.1175/BAMS-D-20-0112.2

In final form 3 February 2021

AFFILIATIONS: Lim, Hendon, Dowdy, and Wang—Bureau of Meteorology, Melbourne, Australia; **Butler**—NOAA/Chemical Sciences Laboratory, Boulder, Colorado; **Thompson**—Department of Atmospheric Science, Colorado State University, Fort Collins, Colorado; **Lawrence**— CIRES, University of Colorado, and NOAA/Physical Sciences Laboratory, Boulder, Colorado; **Scaife**—Met Office Hadley Centre, and College of Engineering, Mathematics and Physical Sciences, University of Exeter, Exeter, United Kingdom; **Shepherd**—Department of Meteorology, University of Reading, Reading, United Kingdom; **Polichtchouk**—European Centre for Medium-Range Weather Forecasts, Reading, United Kingdom; **Nakamura**—Research Center for Advanced Science and Technology, University of Tokyo, Tokyo, Japan; **Kobayashi**—Meteorological Research Institute, Japan Meteorological Agency, Tsukuba, Japan; **Comer**—Met Office Hadley Centre, Exeter, United Kingdom; **Coy**—NASA Goddard Space Flight Center, Greenbelt, and Science Systems and Applications, Inc., Lanham, Maryland; **Garreaud**—Department of Geophysics, University of Chile, Santiago, Chile; **Newman**—NASA Goddard Space Flight Center, Greenbelt, Maryland

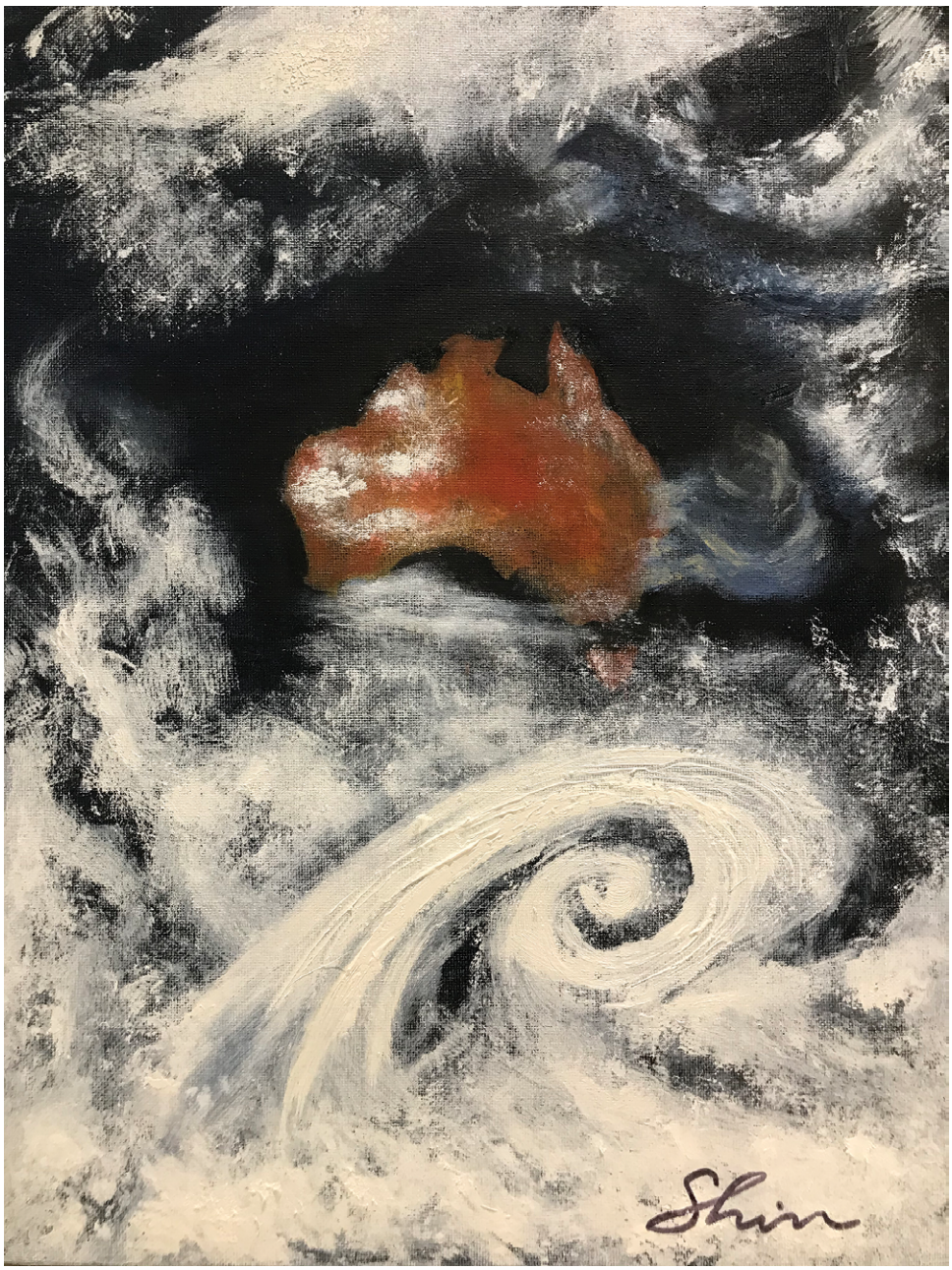

2019 Australian Bushfires seen from space. This painting by Soon Ja Shin was inspired by the satellite picture taken on 5 Dec 2019. The satellite image is publicly available by NOAA https://satellitemaps.nesdis.noaa.gov.

Sudden stratospheric warming events (SSWs) are characterized by dramatic warming and weakening of the stratospheric polar vortex. SSWs have a profound impact on stratospheric circulation and chemical composition and can drive sustained anomalies in surface weather, altering the occurrence of weather and climate extremes (e.g., Kidston et al. 2015; King et al. 2019; Lim et al. 2019), thus serving as an important source of long-range predictability (e.g., Baldwin and Dunkerton 2001; Domeisen et al. 2020). Major SSWs, which are defined by a reversal of the climatological westerly vortex in the midstratosphere followed by a recovery (Charlton and Polvani 2007; Butler et al. 2015), occur every 1–2 years on average in the Northern Hemisphere (NH), but are extremely rare in the Southern Hemisphere (SH): only one major SSW has been observed in the SH over the past ~60 years, which occurred during late September 2002 (e.g., Baldwin et al. 2003; Dowdy et al. 2004; Nishii and Nakamura 2004; Shepherd et al. 2005).

The 2002 SH major SSW, which was a vortex-splitting event, occurred with extraordinarily strong wave forcing from the troposphere throughout the preceding austral winter and the associated contraction of the polar vortex from late winter (e.g., Harnik et al. 2005; Newman and Nash 2005; Scaife et al. 2005). It then dramatically developed over 10 days from 17 September with upper-stratospheric preconditioning (e.g., Newman and Nash 2005; Scaife et al. 2005) and resonant amplification of wave forcing within the stratosphere (Esler et al. 2006), and the wind reversal occurred during 25–30 September. During the 2002 SSW, the stratospheric jet at 10 hPa weakened by 80 m s^{-1} and the Antarctic polar cap (the area mean over 60°–90°S) warmed by 32 K at 30 hPa from 17 to 27 September (NASA Ozone Watch; https://ozonewatch.gsfc.nasa.gov/). These extreme wind and temperature anomalies subsequently coupled downward, leading to the record-strong low polarity (negative) index of the southern annular mode (SAM; Thompson and Wallace 2000) and associated surface climate extremes in the following spring months (Thompson et al. 2005; Hendon et al. 2020).

Beginning in late August 2019, the SH stratospheric polar vortex experienced radical warming and weakening, which was of comparable magnitude to what occurred during 2002, and was displaced from the South Pole (rather than split). Lim et al. (2020) and subsequent studies (e.g., Eswaraiah et al. 2020; Rao et al. 2020; Shen et al. 2020) reported that the stratospheric jet at 10 hPa at 60°S weakened by 80 m s^{-1}, and the polar cap warmed by 35 K at 30 hPa during the 3 weeks following 25 August 2019, setting records for the highest polar cap temperature and weakest westerly jet in the mid- to upper stratosphere in September.

The weakened vortex in September then coupled downward to the troposphere from mid-October to December 2019, with an extraordinarily persistent equatorward shift of the tropospheric eddy-driven westerly jet and a concomitant increase of surface pressure in the polar region and a decrease in the SH midlatitudes. Together these changes characterize a swing to the negative phase of the SAM (hereafter, referred to as negative SAM), which typically follows anomalous springtime weakening of the SH polar vortex, such as those observed in 1988 and 2002 (Thompson et al. 2005; Seviour et al. 2014; Byrne and Shepherd 2018; Lim et al. 2019). The negative SAM in late spring 2019 was record strong for the season and played a significant role in exacerbating the preexisting hot and dry conditions over Australia, which were conducive to the devastating wildfires (known as bushfires in Australia) that ensued along the central east coast (Phillips and Nogrady 2020). It also contributed to below-average rainfall in northeastern Brazil and eastern South Africa, and above-average rainfall in southeastern Brazil, western Patagonia, and southernmost New Zealand during late October through December 2019 (Lim et al. 2020).

Recent studies have already unraveled some key mechanisms that triggered the SSW in mid-September 2019 on daily to weekly time scales (Eswaraiah et al. 2020; Rao et al. 2020; Shen et al. 2020) and have identified significant impacts of this event on the different atmospheric layers and regions (Yamazaki et al. 2020; Noguchi et al. 2020; Wargan et al. 2020; Anstey et al. 2021, manuscript submitted to *Geophys. Res. Lett.*). Here we concentrate on the

low-frequency (i.e., spring season) manifestation of the 2019 SSW, which is, hereafter, referred to as springtime stratospheric polar vortex (SPV) weakening. We show that the origin of this event can be traced back to changes in the polar night jet (PNJ) at the stratopause as early as June 2019 and whose surface impacts were felt through December 2019. We also explore the long-lead predictability of the springtime SPV weakening event using both inferences from lagged statistical relationships based on historical data and coupled model seasonal forecast systems (as opposed to a deterministic prediction of the precise timing of the SSW) and of the sustained surface impacts into austral late spring/early summer 2019. This focus on the monthly to seasonal time-scale evolution of the stratospheric circulation associated with the vortex weakening event and its sustained coupling downward to the surface highlights that springtime SPV variability and associated preconditioning processes are a potential source of predictability of surface climate with lead times much longer than associated with prediction of the abrupt SSW.

For the observational analysis, we have used the Japanese 55-year Reanalysis dataset (JRA-55; Kobayashi et al. 2015) and Global Precipitation Climatology Project (GPCP) precipitation version 2.3 dataset (Adler et al. 2018) for 1979–2019. We computed anomalies for 2019 using the climatology of 1979–2018. For the SPV index and other climate indices, we normalized the index anomalies by their standard deviations (σ) obtained from the climatological 40-yr data. We also analyzed the Australian Water Availability Project (AWAP) gridded analyses (Jones et al. 2009) of Australian temperature and rainfall and a gridded dataset of the McArthur forest fire danger index[1] (Dowdy 2018) to examine the impact of the 2019 SPV weakening on Australian climate in late 2019.

The coupled model seasonal hindcasts for 1990–2012 and real-time forecasts for 2019 were produced from the operational systems of the Australian Bureau of Meteorology (BoM ACCESS-S1; Hudson et al. 2017), the European Centre for Medium-Range Weather Forecasts (ECMWF-SEAS5; Johnson et al. 2019), the Japan Meteorological Agency (JMA/MRI-CPS2; Takaya et al. 2018), NASA (GEOS-S2S-2; Molod et al. 2020), and the Met Office (UKMO GloSea5; MacLachlan et al. 2015). Details of the forecast systems and configurations are described in Table 1.

[1] The McArthur Forest Fire Danger Index (FFDI) was obtained from a dataset as described by Dowdy (2018), based on a gridded analysis of observations at 0.05° in both latitude and longitude throughout Australia. The FFDI is calculated as an exponential function combining relative humidity, temperature, and wind speed as well as a drought factor based on a measure of fuel dryness calculated from antecedent rainfall and temperature. The FFDI has been shown to exhibit predictability on seasonal time scales (Bett et al. 2020), but it is used here as a useful way of combining various weather factors known to influence fire danger and for providing broadscale guidance on climatological features including its relationship to large-scale atmospheric and oceanic modes of variability such as the SAM, stratospheric polar vortex, and El Niño–Southern Oscillation.

Table 1. Details of the five operational dynamical forecast systems and their forecasts used in this study. The UKMO forecast skill indicated by the crosses overlaid with the blue bars in Fig. 9a was computed with the ensemble mean of 21-member forecasts formed with time lags. Asterisk denotes the ensemble formation with two burst members over 4 consecutive days.

Operational centers	Prediction systems	Atmospheric resolution	Available full length of hindcast period	Hindcast Ensemble size per initialization date	2002/2019 forecast ensemble size per initialization date
BoM	ACCESS-S1	N216 L85	1990–2012	11	11
ECMWF	SEAS5	TCo319 (36 km) L91	1981–2019	25 (Jul, Sep) and 51 (Aug	2002: 25 (Jul, Sep) and 51 (Aug) 2019: 51
JMA	JMA/MRI-CPS2	TL159 L60	1981–2014	5	2002: 5 2019: 13
NASA	GEOS-S2S-2	0.5° lat–lon L72	1981–2019	1	1
UKMO	GloSea5	N216 L85	1993–2016	7	2002: 7 2019: 8*

Setting new records

The PNJ, the Antarctic temperatures, and the SAM were all severely disrupted in association with the 2019 SPV weakening. Figure 1a shows Antarctic circumpolar zonal wind anomalies at 60°S (shading) for 1 June to 31 December 2019 (1000 to 1 hPa) superimposed on the climatology (contours). The sudden and massive vortex weakening in the upper stratosphere began in late August and then extended downward into the troposphere from October through the end of December, manifested as persistent period of strong negative SAM (Fig. 1b), which is monitored with the NOAA Climate Prediction Center (CPC) Antarctic Oscillation (AAO) index (available at www.cpc.ncep.noaa.gov/products/precip/CWlink/daily_ao_index/aao/aao.shtml; Thompson and Wallace 2000). Concomitant with the vortex weakening, the polar cap temperature rapidly increased in the upper to midstratosphere and then stayed significantly warmer than normal in the lower stratosphere through December (Fig. 1c). Consistent with thermal-wind balance, the maximum warm anomalies sit below the maximum easterly anomalies. By comparing to the climatological zonal wind, the springtime SPV weakening of 2019 can be viewed as an accelerated march of the seasonal cycle of the SH stratospheric circulation, resulting in an earlier-than-normal breakdown of the winter vortex (e.g., Shiotani et al. 1993; Taguchi and Yoden 2002; Hio and Yoden 2005; Byrne and Shepherd 2018).

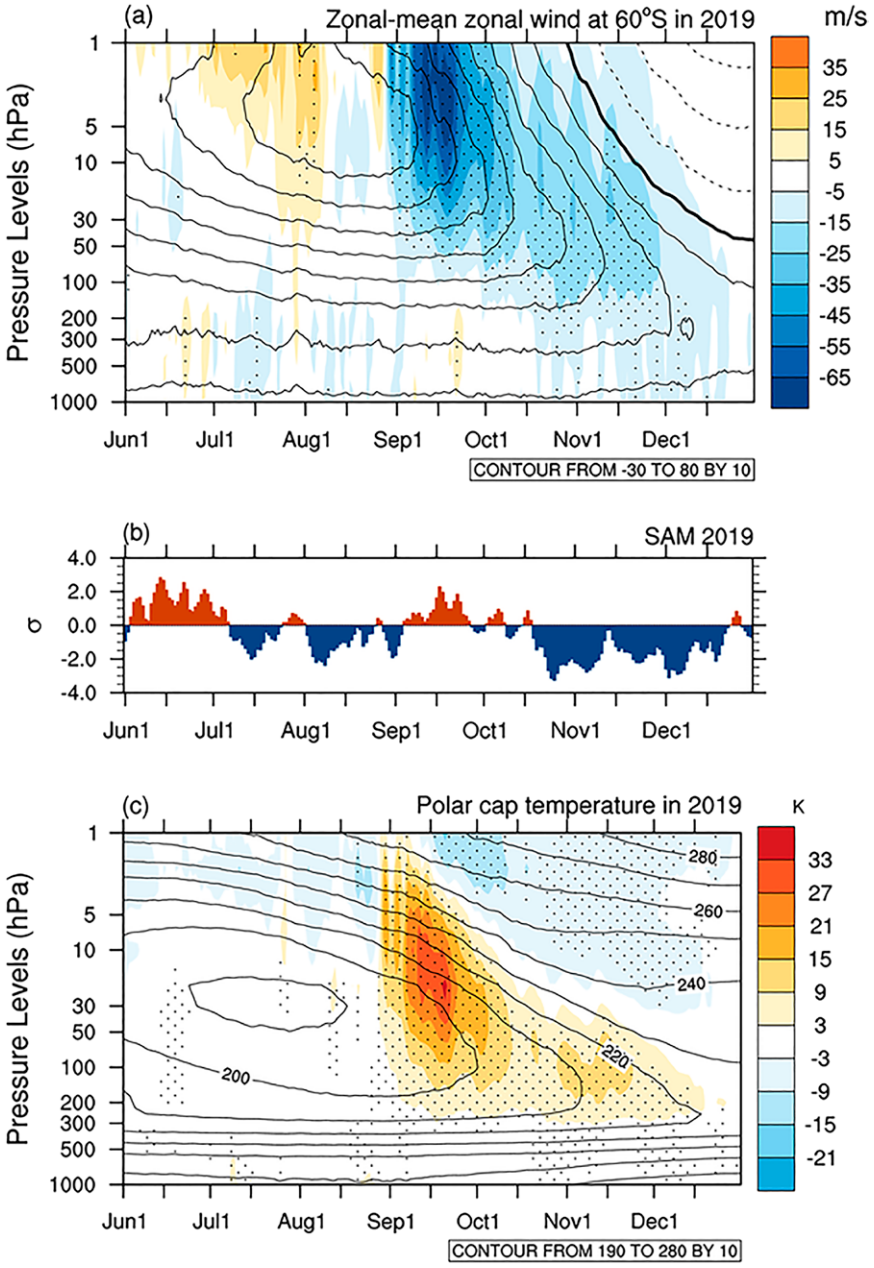

Fig. 1. Daily anomalies of (a) zonal-mean zonal wind ([*U*]′) at 60°S from 1000 to 1 hPa, (b) SAM as monitored by the Antarctic Oscillation (AAO) index by CPC, and (c) Antarctic polar cap temperatures averaged over 60°–90°S. Time runs from 1 Jun to 31 Dec 2019. The daily CPC AAO index in (b) is obtained by projecting daily 700-hPa geopotential height (Z700) anomalies onto the leading mode of the EOF of monthly mean Z700 variability over the domain 20°–90°S (Thompson and Wallace 2000). In (a) and (c) color shading indicates anomalies, and the overlaid contours indicate the climatologies computed over 1979–2018. Color shading intervals are 10 m s^{-1} and 6 K, and contour intervals are 10 m s^{-1} and 10 K for (a) and (c), respectively. Stippling in (a) and (c) denotes the 2019 anomalies fall in the ±5% tails of the climatological distribution as judged by the anomalies being greater than 1.68 standard deviations (σ) or less than –1.68σ, where σ is computed over 1979–2018.

Although the 2019 SSW did not experience a zonal wind reversal at 60°S and 10 hPa to qualify as a major SSW (e.g., Butler et al. 2015), many other measures point to this event

being of record strength, especially when viewed on longer (monthly to seasonal) time scales. For example, the austral springtime mean (September–November; SON) zonal-mean zonal wind ([U]) at 60°S and 1 hPa was the weakest on record by a big margin over the previous records (–3σ compared to –2σ in 1988 and 2002) (e.g., Eswaraiah et al. 2020), and the weakening of [U] at 60°S and 10 hPa was on a par with 2002, with a magnitude of –3σ (Fig. 2b). Similarly, the amplitude of the leading empirical orthogonal function (EOF) of Antarctic polar cap geopotential height anomalies at 30 hPa, which depicts the earlier/later breakdown of the SH stratospheric polar vortex (Byrne and Shepherd 2018), was 2.3σ in both 2002 and 2019 (see Figs. S1a,b in the supplemental material). Likewise, the record magnitude of 2.5σ was exhibited in both years by the leading time–height EOF of Antarctic circumpolar zonal wind, which also captures the variability of the canonical life cycle of the SH stratospheric vortex weakening and its downward coupling to the troposphere that typically evolves from early winter at the stratopause to summer at the surface (Lim et al. 2018; Figs. S1c,d).

There were two records related to the SPV weakening: springtime polar stratospheric temperatures and ozone concentrations were both at record highs—resulting in a very small Antarctic ozone hole. The record-high temperatures were especially evident in the midstratosphere (30 hPa), where the polar temperature anomaly was about 50% higher than in 2002 (Fig. 2c). Typically, Antarctic polar cap ozone increases as the SH stratospheric polar vortex weakens and warms (e.g., Stolarski et al. 2005; Keeble et al. 2014; Seviour et al. 2014). The strengthened Brewer–Dobson circulation associated with the 2019 SPV weakening (Noguchi et al. 2020) transported midstratospheric

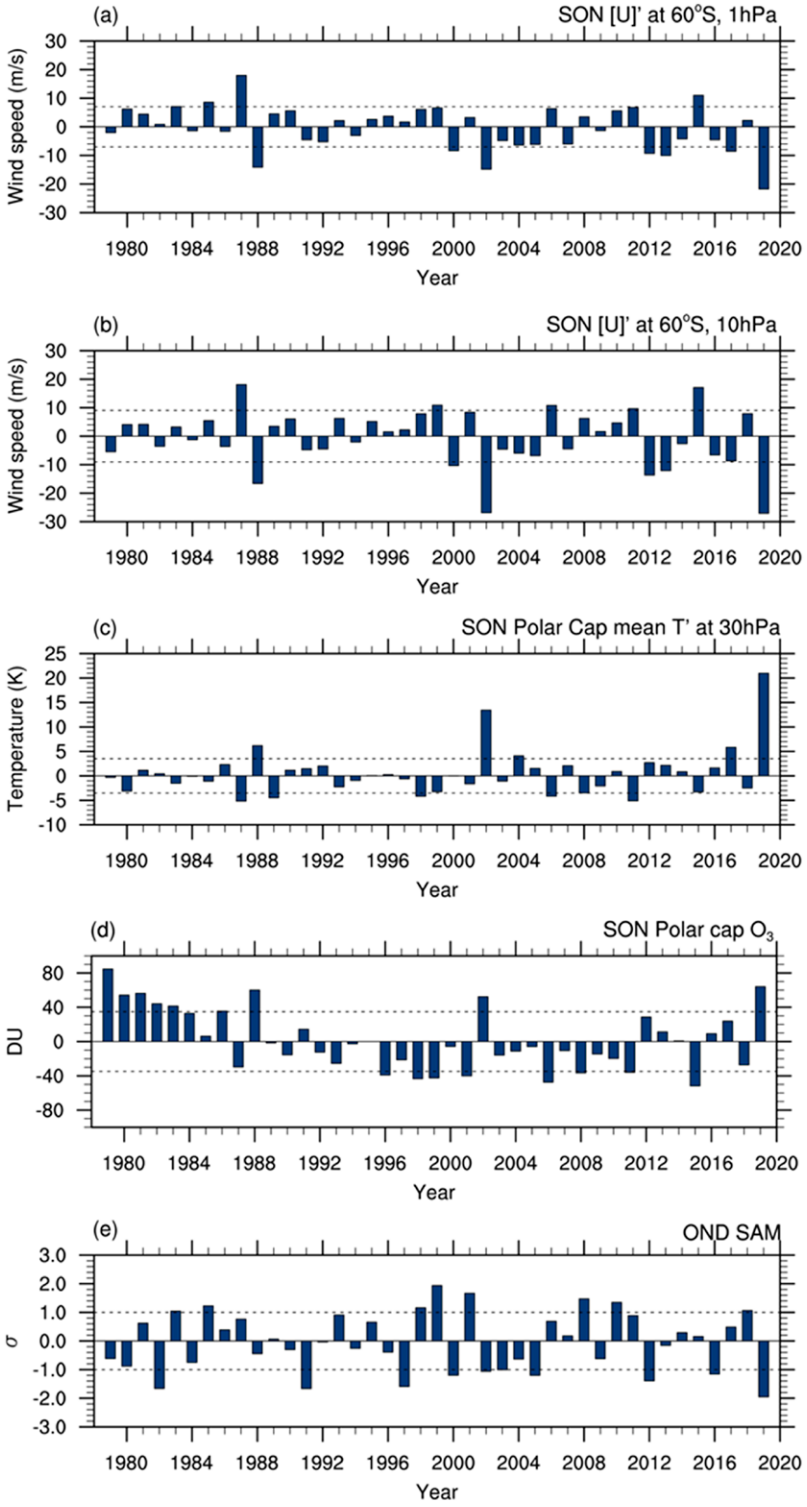

Fig. 2. Time series of anomalies of (a) SON [U]′ at 60°S at 1 hPa. (b) As in (a), but at 10 hPa (i.e., the SPVI). (c) SON Antarctic temperature south of 60°S at 30 hPa. (d) SON Antarctic polar cap ozone [the data of total column ozone averaged over the polar cap south of 63°S were obtained from the NASA Ozone Watch page (https://ozonewatch.gsfc.nasa.gov/)]. (e) Standardized OND-mean SAM (NOAA CPC monthly AAO) index. The dashed horizontal lines in each panel indicate a unit standard deviation.

ozone from the midlatitudes into the polar region, while also developing an enhanced downward circulation that warmed the polar lower stratosphere (Wargan et al. 2020). This warming curtailed the typical chlorine and bromine catalytic ozone loss processes that cause the ozone hole. The polar cap total column ozone concentration in SON 2019 was the highest on record since 1979 (Fig. 2d) primarily due to the SPV weakening (Wargan et al. 2020).

Despite the extraordinarily early start of the 2019 SSW in late August, the wind and temperature anomalies did not couple down to the troposphere until mid-October. However, once the stratosphere–troposphere coupling occurred, the resultant SAM index averaged over October–December was the most strongly negative on record for that season (Fig. 2e), which is consistent with a strong correlation between the October–December-mean SAM index (Fig. 2c) and the springtime SPV index (SPVI, defined here as $[U]$ at 60°S and 10 hPa averaged for the SON season; Seviour et al. 2014) (Fig. 2b) over 1979–2018 ($r \sim 0.66$).

Dynamical processes for the 2019 stratospheric vortex weakening

Before the drastic weakening of the polar vortex in September 2019, the PNJ at the stratopause first shifted poleward during early austral winter (June–July), which is likely due to increased wave forcing in early winter (e.g., Kodera and Kuroda 2002). The evolution of the 2019 vortex weakening and a comparison to historically observed SH springtime SPV events are shown in Fig. 3. The right-hand column displays the 2019 evolution of zonal-mean zonal wind anomalies ($[U]'$) at 1 hPa (near the stratopause), 10 hPa (midstratosphere), and 100 hPa (lower stratosphere) as a function of calendar month. The left-hand column displays the same fields but derived from the regression onto the SPVI displayed in Fig. 2b. The regression coefficient patterns were obtained using data for the period 1979–2018, and the syntheses for 2019 were obtained by multiplying the regression coefficients by the 2019 value of the SPVI to show the evolution of $[U]'$ at these different levels that was expected from the 2019 SPV weakening in spring (see details in the supplemental material).

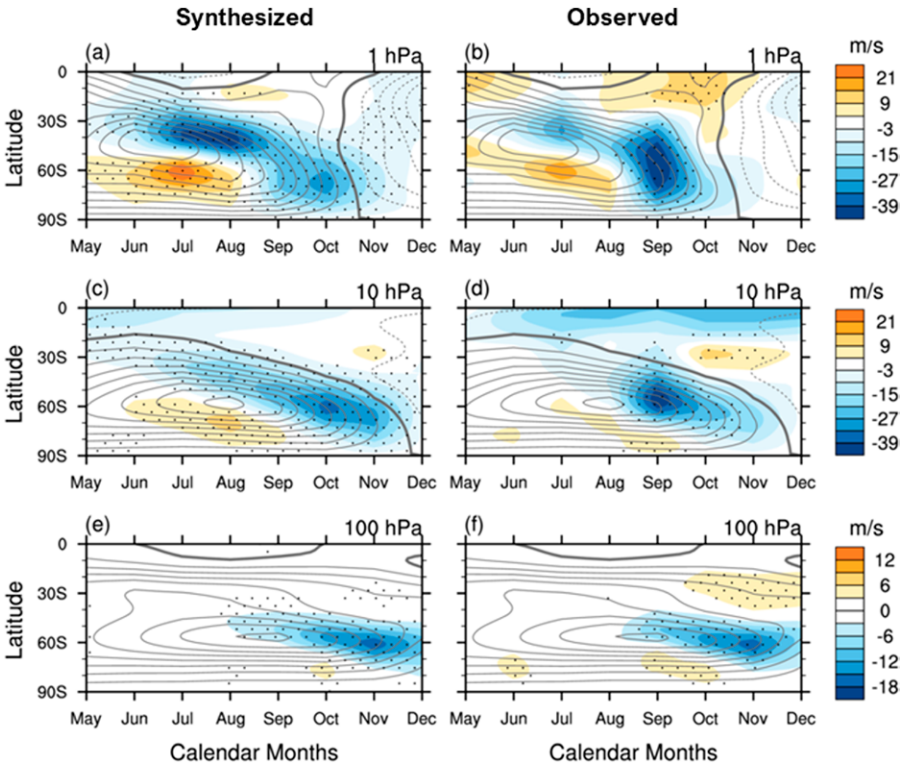

Fig. 3. Latitude–time sections of monthly mean anomalies of zonal-mean zonal wind ($[U]'$) at (top) 1, (middle) 10, and (bottom) 100 hPa. (a),(c),(e) Syntheses of 2019 by regressing $[U]'$ at 1, 10, and 100 hPa onto the SPVI shown in Fig. 2b for 1979–2018 and scaling the regression coefficients by the 2019 index magnitude (see supplemental material for further details). (b),(d),(f) 2019 observed $[U]'$ at 1, 10, and 100 hPa, respectively. Color shading indicates anomalies, and contours indicate the climatological winds. Color shading intervals are 6 m s^{-1} in (a)–(d) and 3 m s^{-1} in (e) and (f), and contour intervals are 10 m s^{-1} in (a)–(d) and 5 m s^{-1} in (e) and (f). Zero contours are thickened and negative contours are dashed. Stippling in the left panels denotes statistical significance of the regression coefficients at the 10% level, assessed by a two-tailed Student's *t* test with 40 samples, and stippling in the right panels denotes extreme anomalies in the ±5% tails of the climatological distribution as described in Fig. 1.

For both the synthesized and observed anomalies of 2019, the development of easterly anomalies in the mid- and lower-stratospheric polar vortex from September onward can be traced back to a poleward shift (i.e., a meridional dipole anomaly) of the PNJ at 1 hPa during early winter (Figs. 3a,b). This meridional dipole anomaly in the upper-stratospheric westerlies peaks in July and then gradually moves poleward through August in conjunction with the seasonal poleward shift of the jet from winter to spring (e.g., Kodera and Kuroda 2002; Byrne and Shepherd 2018). Beginning in September, the upper-stratospheric wind anomaly takes the form of a monopole weakening of the vortex that extends from 30°S to the pole. This rapid latitudinal expansion of the easterly anomalies in the upper stratosphere in September, reflecting the sustained effects of a weakened vortex, concurs with the appearance of easterly anomalies in the mid- to lower stratosphere that then persist through at least December (Figs. 3c–f).

We note that springtime weakening of the SH polar vortex coincides with easterly anomalies in the low latitudes equatorward of 10°S at 10 hPa in both the canonical development derived from regression and in the 2019 anomalies (Figs. 3c,d). The tropical easterly anomalies at 10 hPa are a signal accompanying the westerly phase of the quasi-biennial oscillation (QBO) defined at 30–50 hPa (e.g., Anstey et al. 2010; Shen et al. 2020; for the QBO in 2019, see https://acd-ext.gsfc.nasa.gov/Data_services/met/qbo/qbo.html). Tropical stratospheric winds could potentially alter wave propagation characteristics and/or the stratospheric residual mean circulation in ways that affect the polar vortex (Holton and Tan 1980; Baldwin et al. 2001; Anstey and Shepherd 2014; Byrne and Shepherd 2018; Gray et al. 2020). Given the statistically significant connection between the easterly signal of the QBO in May and a poleward shift of the westerly jet in the subsequent winter months at 10 hPa (Fig. 3c), an in-depth investigation is warranted for the influence of the QBO-related midstratospheric easterlies on the different stages of the polar vortex evolution during 2019, although Shen et al. (2020) briefly noted that the tropical easterly anomalies at 10 hPa associated with the QBO were unlikely to be a direct cause of the 2019 SSW. On the other hand, Anstey et al. (2021, manuscript submitted to *Geophys. Res. Lett.*) suggest that the 2019 SSW impacted the QBO and its predictability by significantly disrupting the downward propagation of the tropical easterly anomalies to the lower stratosphere.

The preceding poleward shift of the PNJ during austral winter for both the historical development of springtime vortex weakening and the 2019 event is maintained by a similar dipole pattern of anomalous meridional eddy momentum flux convergence in the upper stratosphere (Figs. 4a,b). Anomalous upward flux of wave activity from the troposphere into the stratosphere, as indicated by the poleward eddy heat flux[2] at 100 hPa, develops over 50°–70°S from July and peaks in September (Matsuno 1970; Shiotani et al. 1993; Kuroda and Kodera 1998; Newman et al. 2001; Hio and Yoden 2005) (Figs. 4c,d).

The increased westerlies at 1 hPa (Fig. 3a) and associated increased upward- and equatorward-propagating wave activities in the lower and upper stratosphere, respectively (Figs. 4a,c), all appear on the poleward sides of their climatological maxima during July and August. This is consistent with the concept that poleward movement of the winter PNJ, which happens when Rossby waves break in the subtropical surf zone, acting to sharpen the potential vorticity gradient and causing the polar vortex to shrink toward the pole, may focus upward-propagating wave activity into the polar cap, subsequently acting to weaken the vortex (McIntyre and Palmer 1983; Kodera and Kuroda 2002; Harnik et al. 2005; Albers and Birner 2014; Lawrence and Manney 2020, and references therein). The poleward heat flux anomalies at 100 hPa increase dramatically from July to October (Fig. 4c), and the convergence of this heat flux in the vertical exerts the necessary easterly forcing to weaken the vortex from August onward (Fig. S2). The 2019 anomalies

[2] The poleward eddy heat flux represents the upward flux of wave activity (Newman and Nash 2005). The poleward heat flux is negatively signed in the SH (i.e., northward heat flux being positive).

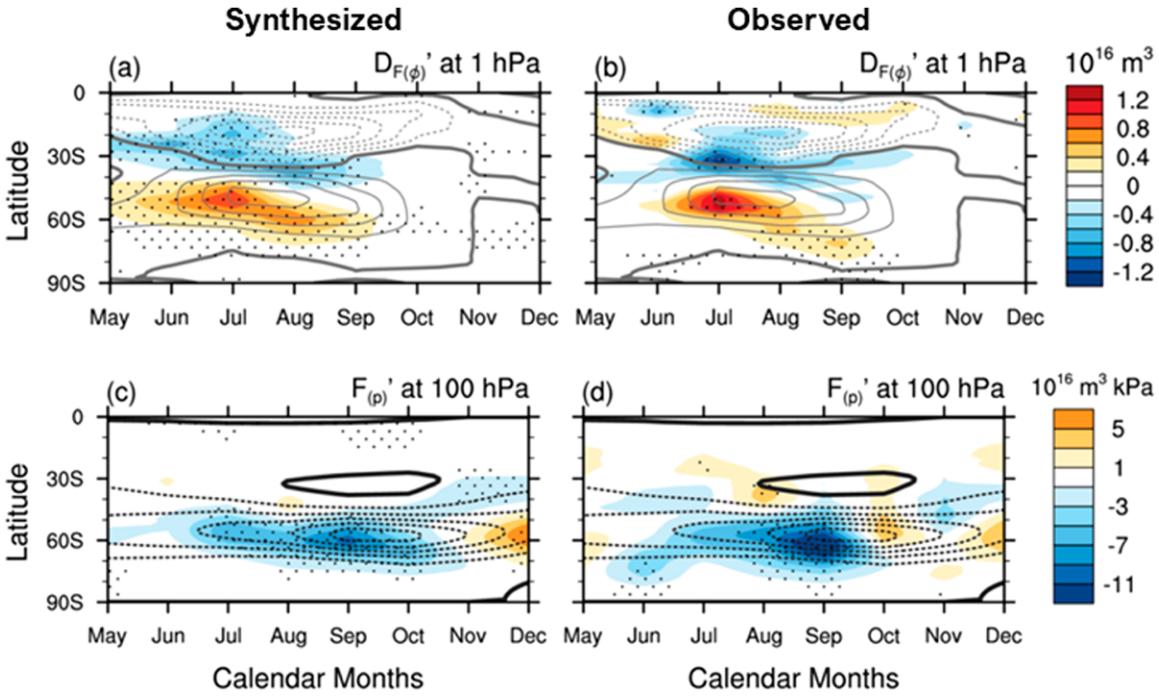

Fig. 4. As in Fig. 3, but for (top) the monthly mean anomalies of Eliassen–Palm (EP) flux divergence ($D'_{F(\phi)}$) by the horizontal component ($F_{(\phi)}$) (i.e., momentum flux convergence) at 1 hPa and (bottom) the vertical component of the EP flux ($F'_{(p)}$) (i.e., poleward eddy heat flux) at 100 hPa. In (c) and (d) negative values indicate the southward (i.e., poleward) heat flux in the SH representing upward wave propagation. The EP flux and its divergence were computed on the spherical coordinate following Peixoto and Oort (1992). Color shading and contours show anomalies and climatologies, respectively, of $D_{F(\phi)}$ and $F_{(p)}$. The color shading interval is 0.2 × 10^{16} m^3 for ($D'_{F(\phi)}$) and 2.0 × 10^{16} m^3 kPa for ($F'_{(p)}$), and the contour interval is 0.2 × 10^{16} m^3 for $D_{F(\phi)}$ and 2.0 × 10^{16} m^3 kPa for $F_{(p)}$. Stippling indicates the statistical significance as described in Fig. 1.

appear to closely follow the canonical evolution of the upper-stratospheric winds and planetary wave activity for springtime polar vortex weakening, but the poleward heat flux anomalies at 100 hPa were extraordinarily strong in August and September 2019 (Fig. 4d), which was consistent with the resultant record weakening of the polar vortex.

More details of the increased poleward heat flux during 2019 are provided in Fig. 5a, which displays the standardized amplitudes of the wave-1 poleward heat flux anomalies averaged over 45°–75°S at different vertical levels during May–December 2019 (Jucker 2016; Birner and Albers 2017). We limit our interest to the wave-1 heat flux as it was the most dominant component in the wave forcing for the 2019 SSW (Rao et al. 2020; Shen et al. 2020), although there was a substantial positive contribution of the wave-2 heat flux in July (Fig. S3). The initial wave-1 poleward heat flux increases in June were confined to the mid- and upper stratosphere, consistent with the poleward contraction of the PNJ as discussed earlier. Subsequently in August and September 2019, extraordinarily strong heat flux anomalies (<–3σ) developed throughout the troposphere and stratosphere (e.g., Milinevsky et al. 2020). This wave-1 heat flux event of August 2019 was the second strongest in the lower troposphere (after 1988) and the strongest at 100 hPa since 1979 (Fig. S4).

Although a growing body of research shows that SSWs can occur without the anomalous upward wave activity flux emanating from the troposphere (e.g., Scott and Polvani 2004; Esler and Scott 2005; Jucker 2016; Birner and Albers 2017), an indication of the tropospheric source of the enhanced upward injection of wave activity (i.e., enhanced poleward heat flux) in late winter 2019 is provided by the August-mean eddy geopotential height averaged over

45°–75°S (Fig. 5b) and 700-hPa geopotential height anomalies (Z700) (Fig. 5c). The observed SH Z700 anomalies in August 2019 are characterized by a primary anticyclonic anomaly over the Bellingshausen–Amundsen Seas and a secondary anticyclonic anomaly in the southern Indian Ocean south of Australia with two cyclonic anomaly centers in between. This pattern strongly projects onto the Z700 anomaly patterns associated with the increase of the wave-1 poleward heat flux at 700 hPa and, to a lesser degree, at 100 hPa (Fig. S5). The eddy geopotential height pattern of 2019 shows that this lower-tropospheric wave pattern propagates upward with a westward tilt, significantly amplifying in the upper stratosphere (Fig. 5b), suggesting that the anomalous tropospheric wave pattern in 2019 was conducive to vertical wave propagation. Rao et al. (2020) and Shen et al. (2020) show that the upward-propagating wave-1 activity further increased in September, playing a key role in the onset of the SSW.

Our preliminary investigation to find possible sources of this extraordinary increase of the wave-1 poleward heat flux hints that convection anomalies over the tropical–subtropical Indian and western Pacific Oceans could have acted as the sources of the teleconnection that promoted the August lower-tropospheric circulation anomaly (Fig. S6). More sophisticated wave analysis and/or carefully designed dynamical modeling experiments would help further elucidate possible tropical influences on the poleward heat fluxes and resultant SH spring vortex variations, which is beyond the scope of this study.

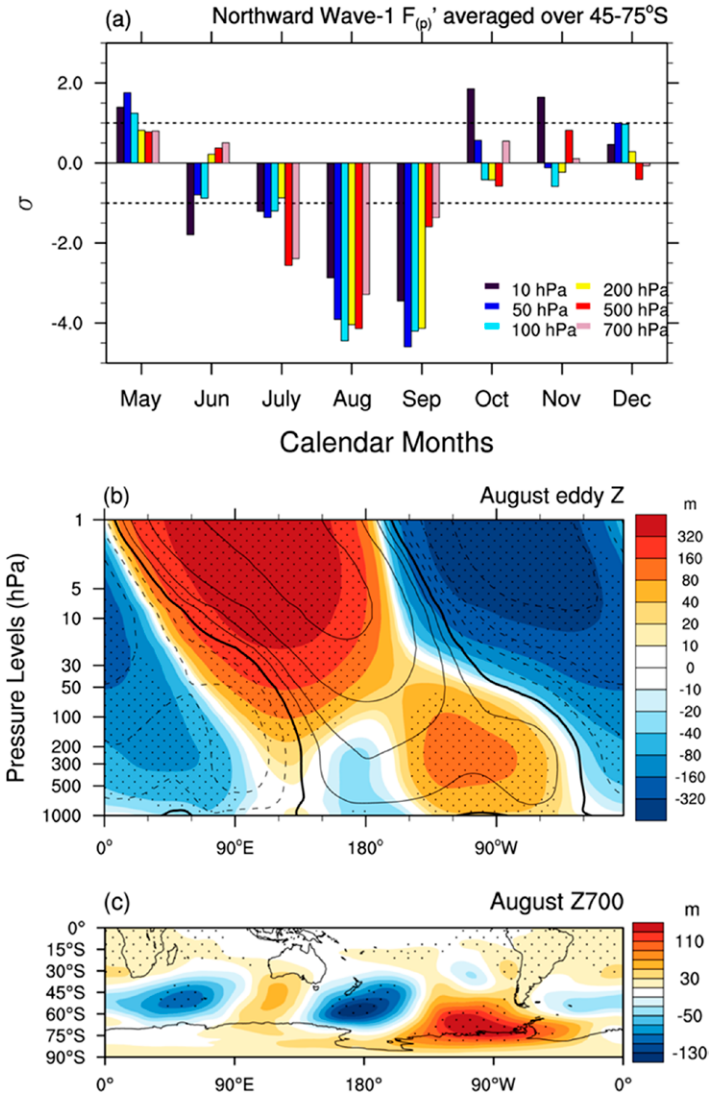

Fig. 5. (a) Standardized anomalies of poleward wave-1 heat flux ($F'_{(p)}$) averaged over 45°–75°S (with cosine latitude weighting) at different vertical levels. (b) August eddy geopotential height (Z) averaged over 45°–75°S (with cosine latitude weighting). The contours and color shading indicate climatological and 2019 eddy patterns, respectively. (c) Z700 anomalies for August 2019. In (b) the color shading interval starts from –10 and 10 m and increases by twofold, and the contour interval does the same but starting from –20 and 20 m. In (c) the color shading interval is 20 m. Stippling in (b) and (c) indicates extremity of anomalies as described in Fig. 1.

Impact on the SH regional climate

The 2019 stratospheric vortex weakening signal descended to the surface from mid-October through December (Fig. 1), setting a new record for negative SAM for that season (Fig. 2e). Negative SAM is characterized by equatorward shifts of the tropospheric eddy-driven westerly jet and associated midlatitude storm track, therefore bringing wet and cold conditions to western Patagonia and southeast South America (SA), western Tasmania, and southern New Zealand and dry westerly winds over southern portions of Australia in the October–December season (OND) as well as in austral summer (e.g., Gillett et al. 2006; Lim et al. 2018; Garreaud 2018). Additionally, negative SAM is accompanied by an equatorward shift of the descending branch of the SH Hadley cell in austral warm seasons (e.g., Kang et al. 2011; Ceppi and

Hartmann 2013; Hendon et al. 2014), therefore resulting in increased downward motion and reduced cloudiness in the SH subtropics and associated dry and warm conditions, which are most prominent over eastern Australia (Lim et al. 2018, 2019).

The SH horizontal and vertical circulation anomalies of OND 2019 closely followed the canonical responses to the springtime SPV weakening, as depicted by regression onto the SPVI (Fig. 6). Although the observed pressure anomalies depict negative SAM (Fig. 6b), they are less zonally symmetric than the canonical response to vortex weakening especially over the central and eastern portions of the South Pacific (Fig. 6a). This feature is largely explained by the presence of central Pacific (CP) El Niño and the extraordinarily strong positive Indian Ocean dipole mode (IOD; Figs. S7a–c), which are monitored by the El Niño Modoki index[3] (EMI; Ashok et al. 2007) and the dipole mode index[4] (DMI; Saji et al. 1999) (Fig. S8), respectively. Both CP El Niño and IOD promote Rossby wave trains that propagate toward the southeast Pacific, thereby contributing to zonally asymmetric circulations in the SH extratropics (Figs. S7d–f; e.g., Ashok et al. 2007; Cai et al. 2011). Consequently, the large-scale circulation anomalies over the southern Atlantic and far eastern Pacific were weaker than those typically observed during the springtime SPV weakening and negative SAM, which led to only moderate wet anomalies in western

[3] $\mathrm{EMI} = \overline{\mathrm{SST}}\mathrm{cp} - 0.5 \times \left(\overline{\mathrm{SST}}\mathrm{ep} + \overline{\mathrm{SST}}\mathrm{wp}\right)$, where cp denotes tropical central Pacific (10°S–10°N, 165°–220°E), ep denotes tropical eastern Pacific (15°S–5°N, 250°–290°E), and wp denotes tropical western Pacific (10°S–20°N, 125°–145°E). The overbar represents the area average.

[4] DMI = $\overline{\mathrm{SST}}$ (10°S–10°N, 50–70°E)– $\overline{\mathrm{SST}}$ (0–10°S, 90–110°E), where the overbar denotes the area average.

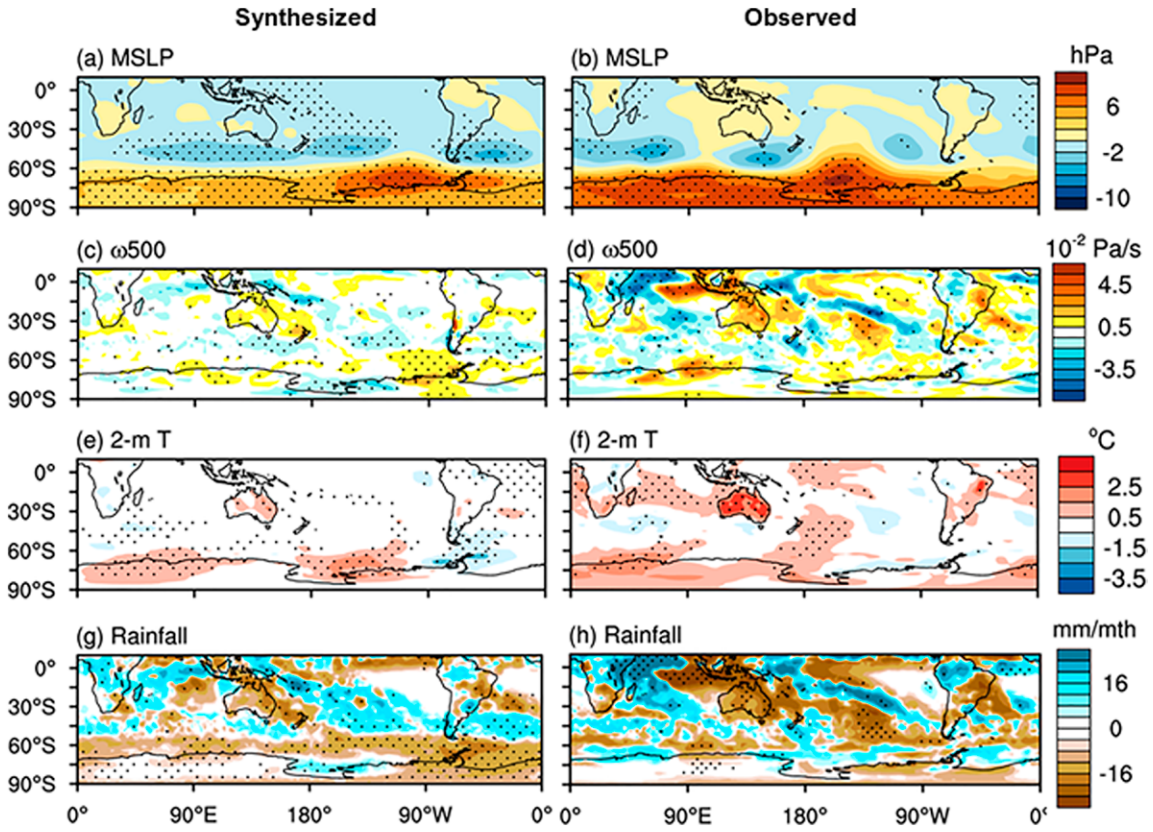

Fig. 6. Syntheses of 2019 OND-mean (a) mean sea level pressure (MSLP), (c) vertical velocity (ω) at 500 hPa, (e) 2-m air temperature, and (g) rainfall anomalies derived from the regression onto the SPVI as described in Fig. 3. The color shading interval is 2 hPa in (a), 0.01 Pa s^{-1} in (c), and 1°C in (e). The color shading interval in (g) increases by twofold for each level from –2 and 2 mm $month^{-1}$. (b),(d),(f),(h) As in (a), (c), (e), and (g), but the observed anomalies of 2019. Stippling indicates the statistical significance as described in Fig. 3, except in (h), where stippling shows where the rainfall anomalies are found in the top- and bottom-decile categories.

Patagonia and cold anomalies in the southern tip of SA and around the Antarctic Peninsula (Fig. 6, right panels). In contrast, a dipole of precipitation and temperature anomalies along eastern SA was prominent in late spring 2019: eastern Brazil was significantly warmer and drier than normal with significantly enhanced downward motion and reduced cloud cover, whereas the opposite conditions occurred in Uruguay and parts of Argentina (Fig. 6d, Fig. S9b). These dipole patterns are similar to those associated with the springtime SPV weakening and negative SAM (Fig. 6c, Fig. S9a) but much more intense.

As broadcast worldwide, eastern Australia suffered from extreme hot and dry conditions and resultant severe wildfires during OND 2019 (e.g., Phillips and Nogrady 2020). Significantly enhanced downward motion, clearer sky, higher temperatures, and lower rainfall over eastern Australia were highly consistent with the anomalies expected to occur during SPV weakening and negative SAM (Fig. 6 and Fig. S9; Lim et al. 2019). Furthermore, the positive IOD in OND 2019 was record strong for the season as evidenced by the DMI being greater than 3σ, and CP El Niño was strong as well, as judged by the EMI being 1σ in NOAA OI v2 SST data (Reynolds et al. 2002) [which was combined with Hurrell et al. (2008) SST data for 1979–81 in our analysis] (Fig. S8). These anomalous SST conditions are well-known drivers of hot and dry conditions over Australia in its spring season (e.g., Saji and Yamagata 2003; Wang and Hendon 2007; Cai et al. 2011), providing long-lead predictability. All these extreme large-scale conditions impacted Australian late spring climate on top of its ongoing long-term warming trend, much of which is thought to be anthropogenically driven (Reisinger et al. 2014), and the multiyear drought that had begun in 2017 (www.bom.gov.au/climate/drought/knowledge-centre/previous-droughts.shtml). Together, they resulted in extreme conditions for wildfire occurrence across the country.

To better understand the relative roles of the stratospheric polar vortex weakening (and associated negative SAM), CP El Niño, the positive IOD, and the linear long-term trend for the late spring extreme climate of Australia in 2019, we have synthesized the Australian daily maximum temperature (Tmax), rainfall, and forest fire danger index (FFDI) for late spring (OND) 2019, based on multiple linear regression. For this "storyline" approach (Shepherd 2019), we used four predictors: the detrended EMI and DMI for OND, the detrended SPVI, and time to capture any trend since 1979.[5] Figure 7 shows that all four predictors significantly contributed to the hot, dry, and fire-prone conditions over different parts of Australia. CP El Niño contributed to drier conditions country-wide but especially in the north (Figs. 7a,g,m) while the positive IOD contributed to intense hot, dry, and dangerous fire weather conditions in the southeast (Figs. 7b,h,n). The linear trend since 1979 contributed more modestly to the warming in the southern half of the country while making the northwest wetter (Figs. 7d,j,p). The springtime SPV weakening and associated negative SAM appears to have played the most prominent role in the hot, dry, and fire-conducive weather conditions in subtropical eastern Australia (Figs. 7c,i,o), especially along the eastern seaboard of southern Queensland and New South Wales, where severe wildfires occurred from October to December.[6] For the FFDI averaged east of 150°E (the dashed vertical line in Figs. 7m–r), the SPV weakening contributed 43% (28%) to the reconstructed (observed) anomaly, while CP El Niño, the positive IOD and the linear trend contributed 21%, 24%, and 12% (14%, 16%, and 8%) to the reconstruction (observation), respectively.

Although the reconstructed Tmax, rainfall, and fire danger index reasonably well capture the observed conditions in the east (Fig. 7, right two columns), the hot and dry and forest fire danger anomalies in the north and the west of the country far exceeded the reconstruction based on these four large-scale oceanic and atmospheric drivers over the last 40-yr period.

[5] The EMI and DMI of the October–December mean and the SPVI of September–November mean do not have any significant trends over the study period 1979–2018, and they are not significantly correlated to one another ($p > 0.1$).

[6] www.industry.gov.au/data-and-publications/estimating-greenhouse-gas-emissions-from-bushfires-in-australias-temperate-forests-focus-on-2019-20. Figure 5 in the document shows the areas significantly affected by the bushfires in July 2019 to January 2020. See also Phillips and Nogrady (2020).

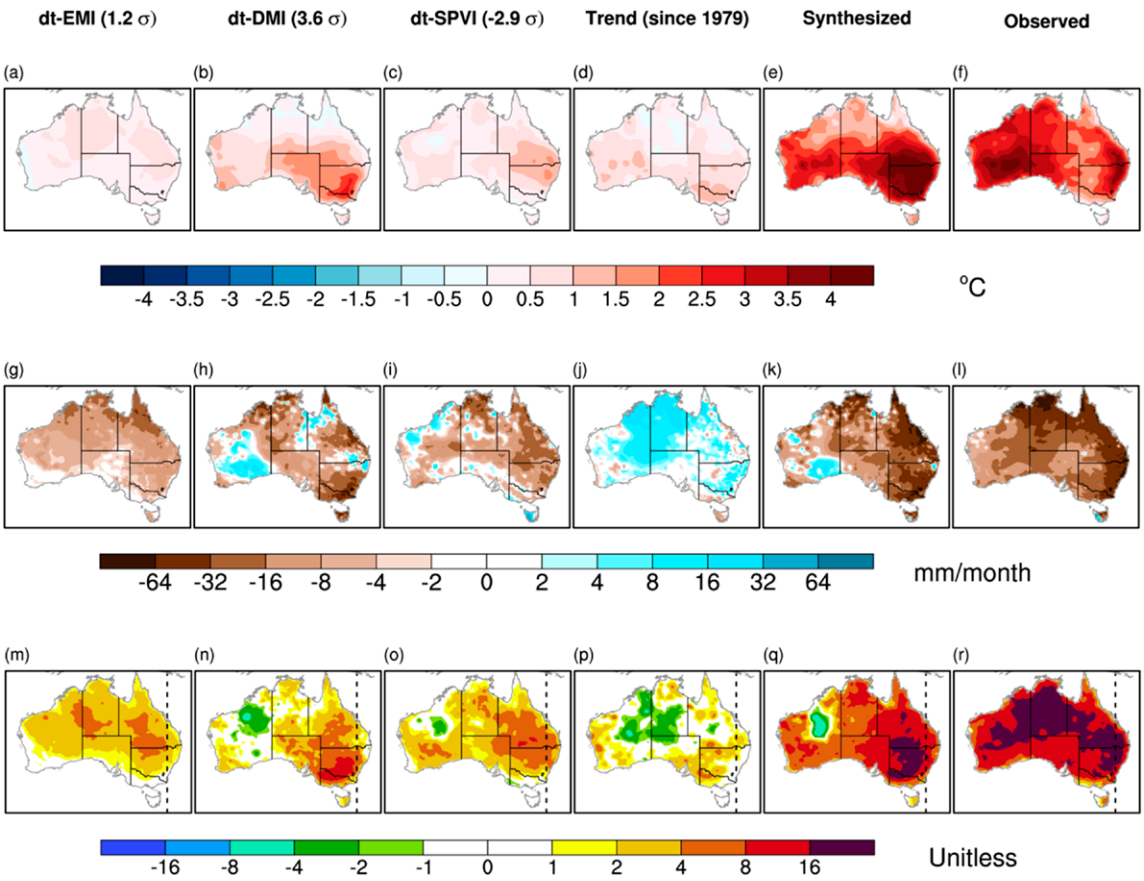

Fig. 7. Patterns of OND-mean Australian (a)–(d) daily maximum temperatures, (g)–(j) rainfall, and (m)–(p) daily forest fire danger index (FFDI) anomalies explained by (a),(g),(m) the detrended El Niño Modoki index (dt-EMI); (b),(h),(n) the detrended Indian Ocean dipole mode index (dt-DMI); (c),(i),(o) the detrended spring polar vortex index (dt-SPVI; Fig. 2b); and (d),(j),(p) a linear trend of OND, using multiple linear regression built for 1979–2018. The regression coefficients are scaled by the 2019 amplitudes of the predictors as indicated by the numbers in the parentheses in the column titles. The synthesized anomalies of 2019 by the multiple linear regression model are displayed in (e), (k), and (q), and the observed anomalies of 2019 are displayed in (f), (l), and (r). The contour interval in (a)–(d) is 0.5°C, while the intervals in (e)–(r) for respective rainfall and FFDI increase by twofold for each level. The dashed vertical line in (m)–(r) marks 150°E as the area east of it experienced intense and prolonged bushfires in the OND season in 2019.

It is important to note that apart from the linear trend shown in Fig. 7, it is challenging to disentangle more complicated potential influences of multiyear to decadal variabilities and climate change on the Australian climate extremes and wildfire risks observed in late spring 2019, which require data of longer records and/or carefully designed dynamical model experiments. Despite this inherent limitation of our simple statistical analysis method, it still provides valuable insight that more than half of the observed forest fire danger risk over the fire-struck region in the far east could be explained by the internally driven dynamical circulation anomalies, and about half of that circulation-driven risk could be explained by the record-strong stratospheric warming event.

Prediction of the 2019 springtime vortex weakening and its impacts

To see how well the 2019 springtime SPV weakening and its impacts on the SH surface climate were predicted, we first consider a multiple linear regression model to predict the SPVI. We use as predictors the PNJ at the stratopause (i.e., $[U]'$ at 60°S, 1 hPa) in June–July and the partial poleward heat flux anomaly at 100 hPa in July–August, which is independent of the June–July

PNJ by regressing out the covarying component with the PNJ from the heat flux anomaly[7] (Fig. 8). Based on the data over 1979–2018, the correlation of the predicted SPVI using the multiple linear regression model with the observed SPVI is 0.73 (using leave-1-yr-out cross validation[8]; Wilks 2006). This statistical model skillfully captures the magnitude of the 2019 event to be comparable to those of 2002 and 1988, the latter being another strong stratospheric warming event with a vortex displacement but without a wind reversal.

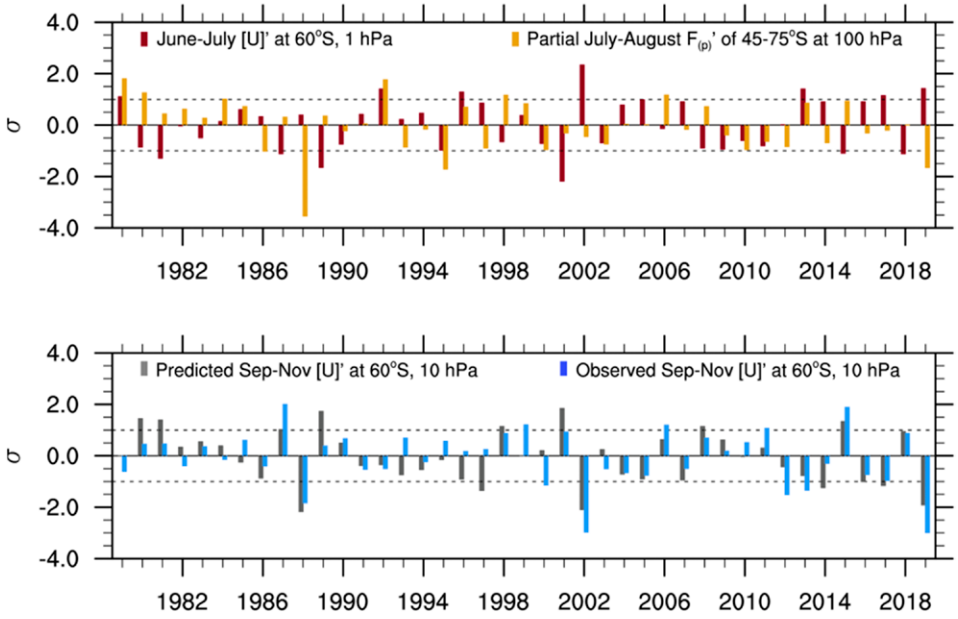

Fig. 8. (top) Time series of June–July mean PNJ ($[U]'$ at 60°S) at 1 hPa (red bars), partial July–August mean northward heat flux ($F'_{(p)}$) independent of the June–July PNJ at 1 hPa (orange bars), and (bottom) statistically predicted SPVI (gray bars). The observed SPVI shown in Fig. 2b is displayed in the bottom panel again with light blue bars for comparison. The time series are normalized by their respective standard deviation (σ) obtained in 1979–2018. The horizontal dashed lines indicate $|1\sigma|$.

A linear regression model with a single predictor, either the June–July PNJ or the July–August 100 hPa poleward heat flux, provides prediction skill of 0.63. However, the June–July PNJ alone underestimates the magnitudes of the 2019 and 1988 events (Fig. 8), while the July–August poleward heat flux alone underestimates the magnitude of the 2002 event. Therefore, this statistical model confirms that both the preconditioning provided by the poleward shift of the PNJ in early winter and subsequent anomalous wave activity flux from the troposphere into the stratosphere in late winter were important for the development of sustained weakening of the SH polar vortex in spring.

Predictability of SPV variability is further assessed using state-of-the-art dynamical seasonal forecast systems (Table 1). Our skill assessment is based on hindcasts over 1990–2012 (with a simple bias correction of using each model's anomalies relative to its climatology as a function of forecast lead time). Using the hindcasts, the SPVI is predictable, as judged by temporal correlation skill (r) being 0.42, which is statistically significant at the 5% level (assessed by a two-tailed Student's t test with 23 independent forecast samples) from as early as 1 July, and is skillfully predictable ($r > 0.6$) from early August (Fig. 9a; see also Seviour et al. 2014; Byrne et al. 2019; Hendon et al. 2020).

For the 2019 springtime SPV, the JMA, UKMO, and ECMWF systems started showing a sign of the weakening for forecasts initialized at the beginning of July (Fig. 9b). Most of the systems predicted a substantially weaker vortex ($<-1\sigma$) for initializations in late July and an extraordinary weakening ($<-2\sigma$) for initializations in late August, although there was a drop in predictability in early to mid-August. From the time when the vortex started its sudden weakening and warming in the observations (i.e., late August to early September), the BoM and UKMO systems, which are based on the same model, overpredicted the vortex weakening and the

[7] June–July PNJ at 1 hPa and July–August poleward heat flux at 100 hPa is correlated by 0.48. While this covariation is naturally accounted for by multiple linear regression (Panofsky and Brier 1963), we have used the partial poleward heat flux at 100 hPa of July–August to assure the independence of the predictors.

[8] Similar skill is obtained with cross-validation processes leaving 5 or 10 years out.

ECMWF system underpredicted it relative to their standard deviations, while NASA and JMA made skillful forecasts for it (Fig. 9b). In comparison, hindcast predictions for the 2002 spring vortex weakening using the same systems show a similar lead-time dependence with an outstanding performance of the one-member NASA system initialized in mid to late July, which then deteriorates in early to mid-August before recovering in late August (Fig. 9c).

An interesting aspect in Fig. 9 is that predictions for the amplitude of the vortex weakening varied by initialization dates only a few days apart for both 2002 and 2019, which highlights the benefit of multiple forecast initialization times during a month and large ensemble sizes to best capture the strength of the SH stratospheric polar vortex. The sharp improvement in the model performance in predicting the strength of the 2019 springtime vortex weakening for forecasts initialized closer to the event suggests that predictability of the actual onset of the sudden warming and subsequent evolution of the polar vortex anomaly throughout spring may be limited by the unpredictable components outside of the deterministic range such as nonlinear wave amplification (e.g., Esler and Matthewman 2011; Sjoberg and Birner 2014; Albers and Birner 2014) or tropospheric noise.

To see if the forecasts for the 2019 springtime SPV weakening correctly represent the proposed low-frequency dynamical processes, we present the BoM forecasts initialized on 25 July 2019, which predicted the SPVI less than -1σ at the earliest (Fig. 9b). The 11-member ensemble mean forecasts captured the increased upward-propagating wave-1 activity and the overall pattern of the lower-tropospheric circulation anomalies in the SH high latitudes (Figs. 10a,b), demonstrating that a sequence of upward-propagating

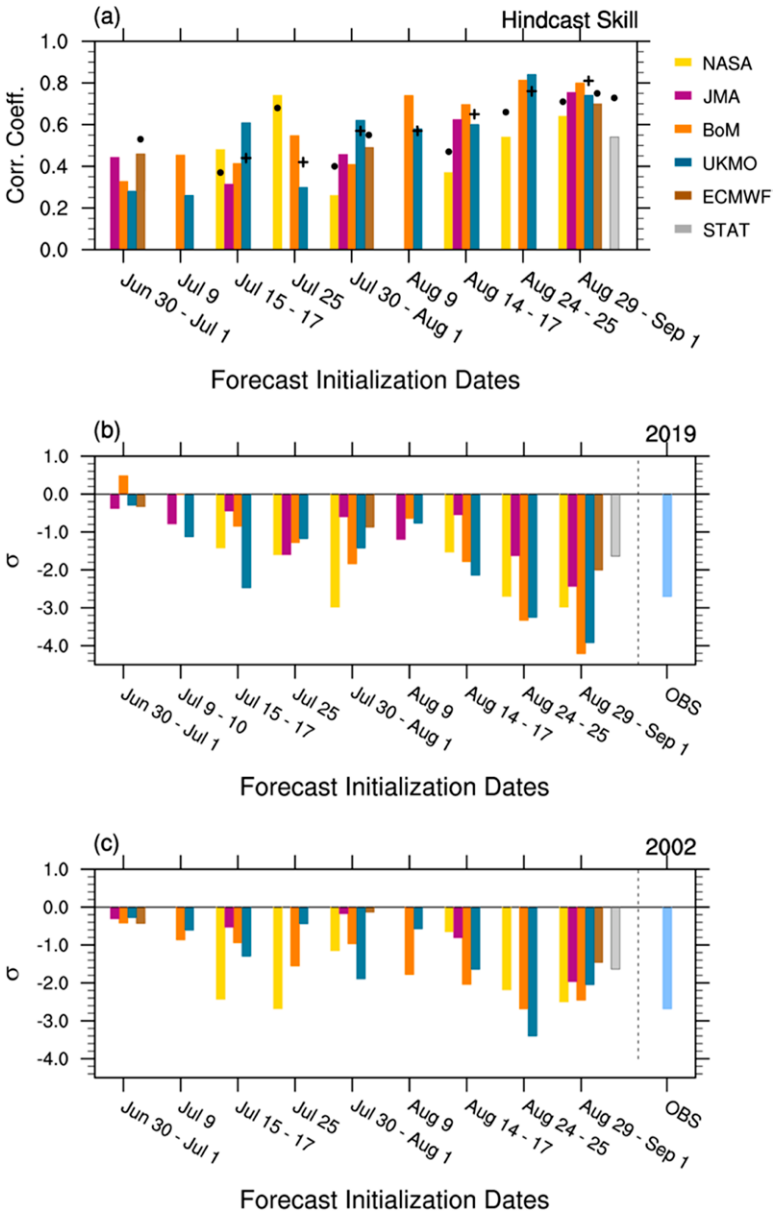

Fig. 9. (a) Hindcast skill to predict the SPVI (as defined with Fig. 2b; SON $[U]'$ at 60°S at 10 hPa) from the five different operational center S2S forecast systems: NASA GEOS-S2S-2 (yellow), JMA/MRI-CPS2 (purple), BoM ACCESS-S1 (orange), UKMO GloSea-5 (blue), and ECMWF-SEAS5 (brown). Skill of the statistical prediction discussed with Fig. 8 is displayed with gray bars. All colored bars, except for the blue bars (UKMO), represent the hindcast skill obtained over 1990–2012, for which the statistical model was rebuilt. The hindcast skill of the UKMO system was computed over 1993–2016. Black dots indicate the skill obtained over longer hindcast periods (see Table 1). The crosses overlaid with the blue bars indicate the skill with an increased ensemble size by using up to 17-day lags (compared to seven-member burst ensemble used for the skill shown with the blue bars). (b),(c) Dynamical and statistical forecasts of standardized SPVI for 2019 and 2002, respectively. The observed anomalies are displayed with light blue bars. All the forecast anomalies were computed with each system's climatological mean and standard deviation from its hindcast periods. The abscissa labels show the forecast initialization dates. Displayed dynamical forecasts are the ensemble mean forecasts (except for NASA forecasts), and details of the forecast systems and ensemble sizes are provided in Table 1.

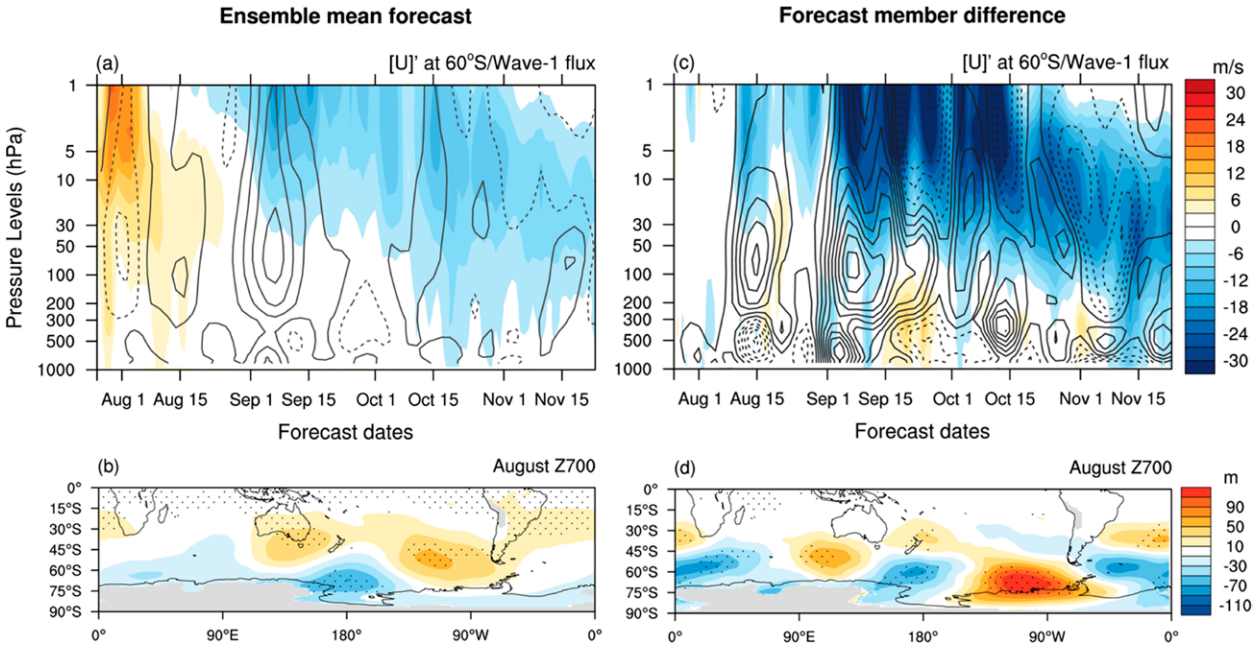

Fig. 10. The 11-member ensemble-mean forecasts of (a) daily $[U]'$ at 60°S (color shading) overlaid with standardized upward wave-1 activity flux ($F'_{(p)}$) (contours) and (b) August-mean Z700 anomalies (color shading) from the BoM system. Forecasts were initialized on 25 Jul 2019. In (a) the solid (dashed) thick contour indicates the poleward (equatorward) heat flux and so upward (downward) wave propagation. Normalization of the wave activity flux by its standard deviation was done at each vertical level. Stippling in (b) indicates anomalies at the ±5% tails of the climatological distribution of BoM hindcasts. (c),(d) As in (a) and (b), respectively, but for the mean differences between the three forecast members of the weakest spring polar vortex and those of the strongest spring polar vortex. The color shading interval is 3 m s^{-1}, and the contour interval is 1σ starting from –11.5σ in (a) and (c). The color shading interval is 20 m in (b) and (d). Stippling in (d) indicates statistical significance on the difference of the two means at the 10% level, assessed by a two-tailed Student's *t* test with the sample size of three in each group.

wave events from the lower troposphere acted to slow the upper-stratospheric westerly jet. We further identified the three ensemble members that predicted the least weakening of the springtime polar vortex (mean of 46 m s^{-1}) and the three ensemble members that predicted the most weakening (mean of 27 m s^{-1}). We then formed the mean differences of $[U]$ at 60°S, the wave-1 activity flux, and August-mean Z700 between the two groups. The differences show that stronger predicted vortex weakening is associated with stronger anomalies of upward wave-1 activity flux (Fig. 10c), consistent with the notion that the abrupt warming and deceleration of the vortex were driven by the anomalous upward wave flux. Interestingly, the Z700 difference pattern for the three weakest and strongest vortex forecasts (Fig. 10d) more highly resembles the observed anomaly pattern than the ensemble-mean anomaly pattern does (Fig. 10c), providing reassurance that more vigorous wave-1 activity injected from the particular lower-troposphere anomaly pattern depicted in Fig. 10d is associated with a considerably weaker springtime polar vortex. However, this analysis of ensemble spread implies that, although the model confirms the proposed dynamics for the vortex weakening event taking a season, the precise prediction of the magnitude and timing of the SSW was not predictable at this relatively long lead time because of the stochastic nature of the upward wave activity flux.

We also examine the predictability of the SH surface climate anomalies in October to December 2019 that were promoted by the stratosphere–troposphere coupling in BoM forecasts. As the BoM system skillfully predicted the springtime SPV weakening with the initial conditions from late July, this system could make forecasts for the OND-mean negative SAM with initial conditions of late July onward (Fig. 11a). However, the prediction

initialized on 9 August 2019 failed to produce the negative SAM because only a small reduction in the vortex strength was predicted (Fig. 9b), which implies the dependence of the predictability of late spring SAM on the predictability of the stratospheric polar vortex weakening. The 66 BoM forecasts from the six different initialization dates from late July until early September, represented by different color bars in Fig. 11a, further demonstrate a good linear fit between the forecasts of the springtime SPV weakening and OND negative SAM strengths (Fig. 11b).

We have shown in Figs. 6 and 7 that the SPV weakening and resultant negative SAM was a key driver of the extreme hot and dry conditions over subtropical eastern Australia, which contributed to one of Australia's worst wildfire seasons over the far eastern seaboard. To confirm that relationship in the prediction, we have plotted the forecast OND-mean SAM versus the forecast OND-mean Tmax and rainfall averaged over eastern Australia (east of 140°E) in Figs. 11c and 11d, respectively, using the 55 BoM forecasts initialized on 25 August and 1, 9, 17, and 25 September. The figures suggest that the more negative the SAM was, the hotter and drier eastern Australia was in the forecasts, as evidenced by the correlation of the forecast SAM with the forecast Tmax and rainfall being −0.41 and 0.44, respectively (statistically significant at the 0.2% level). These correlations represent independent evidence of the causal

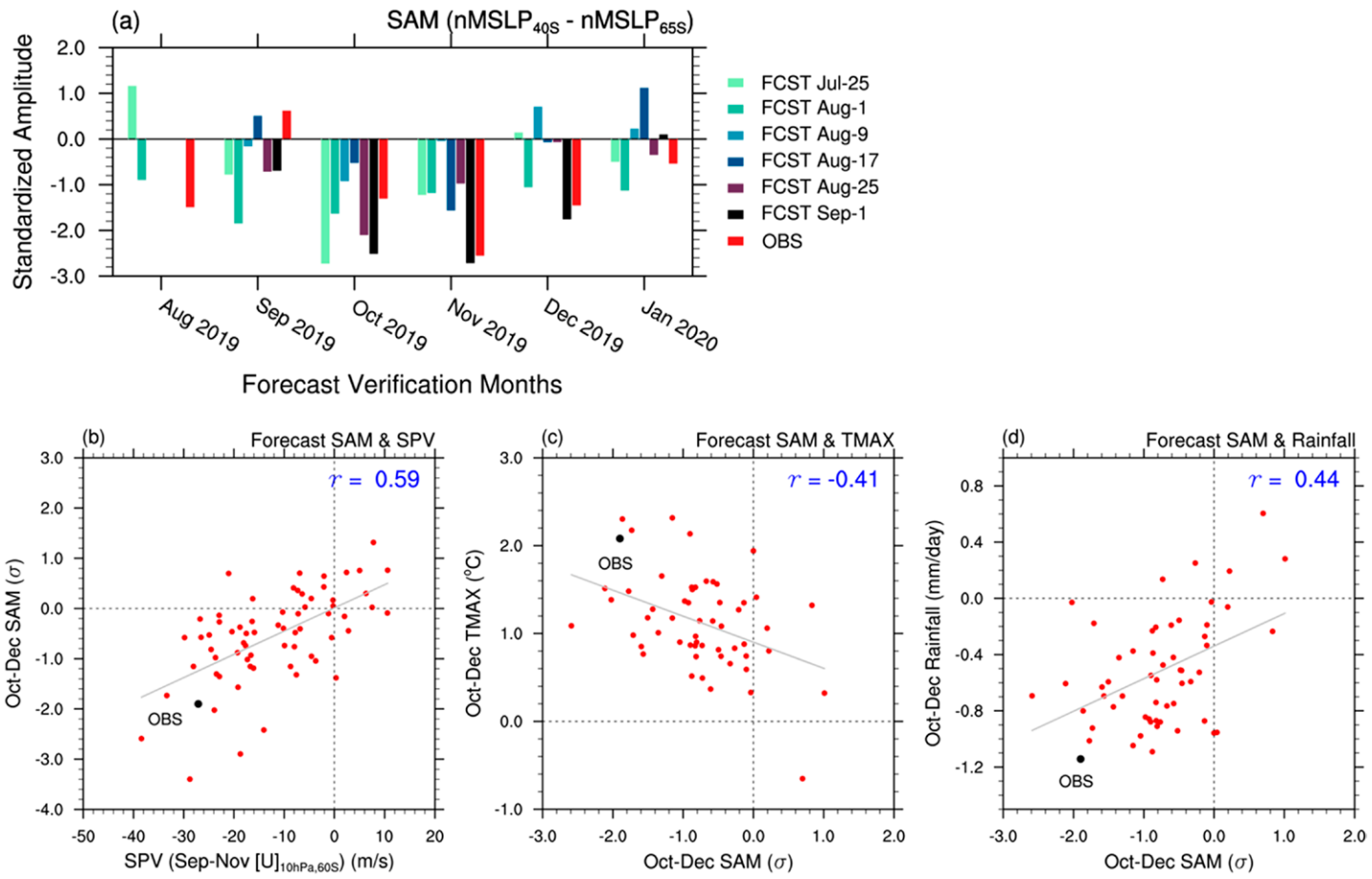

Fig. 11. (a) BoM 11-member ensemble-mean forecasts of monthly SAM initialized on 25 Jul; 1, 9, 17, and 25 Aug; and 1 Sep of 2019. The forecast SAM values were computed by the normalized MSLP difference between 40° and 65°S following Gong and Wang's (1999) definition. The red color bars indicate the observed SAM values obtained from the British Antarctic Survey (www.nerc-bas.ac.uk/icd/gjma/sam.html), which was computed in the same way as Gong and Wang's (1999) method, but with station data (Marshall 2003). (b) The 66 ensemble member forecasts (red dots) initialized on the dates shown in (a) for the SPVI and OND-mean SAM. The observed values are displayed with the black dot. (c),(d) Relationship of the SAM with eastern Australian Tmax and rainfall (east of 140°E and covering 10°–45°S), respectively, in 55 forecasts (11 members initialized on 25 Aug and 1, 9, 17, and 25 Sep 2019) for the OND season.

effect of the SAM on these impact-relevant quantities because the SAM is not strongly correlated with CP El Niño or the IOD in those forecasts. These relationships between the SAM and eastern Australian Tmax and rainfall forecasts of OND are found in the ECMWF forecasts as well with even stronger correlations (Fig. S10).

Concluding remarks

Seventeen years after the first-ever observed major SSW over Antarctica in late September 2002, an equivalently spectacular weakening and warming of the stratospheric polar vortex occurred in September 2019. The impact of the event on the SH surface climate lasted until the end of December. Thanks to advances in the capability of dynamical forecast systems and accumulated knowledge concerning the dynamics and impacts of SH stratospheric polar vortex variability since the 2002 SSW, the 2019 SSW received timely attention from researchers and forecasters, who were able to warn from late austral winter that there would be a high chance of its occurrence with potentially significant impacts on the SH surface climate throughout spring to the end of 2019 (Milinevsky et al. 2020; Hendon et al. 2019a,b). A review of the BoM service for 2019 reports "the BoM provided at least 104 briefings to governments, emergency services and likely affected sectors around the outlook for the fire season (spring and summer). It was recorded that in the 2019 fire season around 19 million hectares were burnt and 33 lives were lost. While horrific, these numbers may have been considerably higher without strategic decisions made through the close information sharing partnerships between the Bureau, Government and emergency services" (Operational Climate Services, BoM, 2020, internal communication).

In this study, we have provided a comprehensive overview of the monthly to seasonal time scale dynamics, climate impacts, and predictability of this remarkable event. Key findings are as follows:

- The 2019 springtime stratospheric polar vortex weakening was as strong as that of 2002 despite not qualifying as a major SSW. New records were set in spring 2019 for the vortex weakening at the stratopause, the Antarctic warming in the midstratosphere, and the high ozone concentration.
- The 2019 event closely followed the canonical development of SH springtime stratospheric polar vortex weakening events with a poleward shifted polar night jet in early winter and record-high monthly mean upward propagating wave-1 activity in August, which emanated from the lower troposphere with distinctive anticyclonic circulation anomalies centered over the Bellingshausen–Amundsen Seas.
- The 2019 stratospheric vortex weakening and warming coupled down to the surface from mid-October, and the resultant record-negative SAM induced significant local climate extremes over eastern Australia, southern New Zealand, eastern South America, and western Patagonia through December 2019.
- Among the well-known large-scale drivers of Australian climate for its warm seasons, the SH springtime polar vortex weakening appears to have been the most influential contributor to the hot and dry and therefore fire-prone climate conditions over the subtropical eastern seaboard of Australia, which suffered from severe and prolonged wildfires during the late spring and early summer period.
- The occurrence of the 2019 springtime stratospheric vortex weakening was foreseeable from July, and its extreme amplitude was skillfully predicted from late August by the state-of-the-art forecast systems analyzed in this study.
- The skillful prediction of the 2019 springtime stratospheric vortex weakening resulted in the skillful prediction of the late spring negative SAM, whose strength was tied to the strength of hot and dry forecasts over eastern Australia for late spring.

We have covered some key aspects of the 2019 stratospheric polar vortex weakening, but many interesting details of this event remain to be explored. For example, we reported substantial amplitude of the wave-2 heat flux in July, but its source, interaction with wave 1, and contribution to the vortex weakening are yet to be understood. Also, Hurwitz et al. (2011, 2014) and Lim et al. (2018) showed a possible relationship of the Antarctic stratospheric warming with central Pacific El Niño, which was present in 2019. Furthermore, the strong positive IOD and associated Rossby wave train was a dominant feature in the SH troposphere in late winter to early spring and might have interacted and/or interfered with the 2019 stratospheric vortex weakening and its downward coupling (e.g., Lim et al. 2020). Thus, atmospheric model experiments forced with the observed versus climatological boundary conditions may shed some light on the role of the extraordinary SST conditions of 2019 for the different stages of the 2019 stratospheric vortex evolution.

Finally, the near-record polar cap total column ozone concentration observed in spring 2019 appears to be largely driven by the stratospheric polar vortex weakening and record warming (e.g., Salby et al. 2002; Randel et al. 2002; Wargan et al. 2020), but ozone variations associated with the stratospheric polar vortex variations can feedback onto the circulation and temperature changes and amplify the impact of the vortex anomalies on the SAM in the troposphere (Hendon et al. 2020). Thus, how much of the negative SAM and associated SH surface climate extremes of October–December 2019 was driven by the ozone increase will be an interesting question to address, which will potentially benefit the future development effort of dynamical seasonal forecast systems, in which ozone is currently prescribed with monthly climatology (e.g., Seviour et al. 2014; Hendon et al. 2020) or radiatively not interactive (e.g., Johnson et al. 2019).

Acknowledgments. This study is part of the Forewarned is Forearmed project, which is supported by funding from the Australian Government Department of Agriculture as part of its Rural R&D for Profit programme. D. W. J. Thompson was supported by the NSF Climate and Large-Scale Dynamics Program. A. Scaife and R. Comer were supported by the Met Office Hadley Centre Climate Programme funded by BEIS and Defra. P. A. Newman and L. Coy were supported by the NASA's Atmospheric Composition Modeling and Analysis Program. A. J. Dowdy was supported by the Victorian Government (DELWP) and Bushfire and Natural Hazards CRC project ERP14. H. Nakamura was supported by JSPS KAKENHI Grant P19H05702, Environment Research and Technology Development Fund (2-1904), ArCS-II Project (MEXT) and JST Belmont Forum CRA "InterDec." The authors are grateful to three anonymous reviewers for their thorough assessments and constructive feedback on the manuscript and to Professor Andrew Dessler for his editorial effort for the peer-review process. Lim and Hendon thank their BoM colleagues Matthew Wheeler and Hanh Nguyen for their constructive feedback on the initial version of the manuscript and Griffith Young and Morwenna Griffith for processing the BoM forecast data and the AWAP data, and thank Kelsey Druken at the National Computing Infrastructure (NCI) for her assistance with the BoM data archiving. This research was undertaken at the NCI National Facility in Canberra, Australia, which is supported by the Australian Commonwealth Government. The NCAR Command Language (NCL; http:// www.ncl.ucar.edu) version 6.4.0 was used for data analysis and visualization of the results. We also acknowledge NCAR/UCAR, NOAA/OAR/ESRL PSL, and the Japan Meteorological Agency for producing and providing the Hurrell et al. (2008) SST analysis, the Reynolds OI v2 SST analysis, GPCP v2.3 precipitation dataset, and the JRA-55, respectively.

References

Adler, R., and Coauthors, 2018: The Global Precipitation Climatology Project (GPCP) monthly analysis (new version 2.3) and a review of 2017 global precipitation. *Atmosphere*, **9**, 138, https://doi.org/10.3390/atmos9040138.

Albers, J. R., and T. Birner, 2014: Vortex preconditioning due to planetary and gravity waves prior to sudden stratospheric warmings. *J. Atmos. Sci.*, **71**, 4028–4054, https://doi.org/10.1175/JAS-D-14-0026.1.

Anstey, J. A., and T. G. Shepherd, 2014: High-latitude influence of the quasi-biennial oscillation. *Quart. J. Roy. Meteor. Soc.*, **140**, 1–21, https://doi.org/10.1002/qj.2132.

——, ——, and J. F. Scinocca, 2010: Influence of the quasi-biennial oscillation on the extratropical winter stratosphere in an atmospheric general circulation model and in reanalysis data. *J. Atmos. Sci.*, **67**, 1402–1419, https://doi.org/10.1175/2009JAS3292.1.

Ashok, K., S. K. Behera, S. A. Rao, H. Weng, and T. Yamagata, 2007: El Niño Modoki and its possible teleconnection. *J. Geophys. Res.*, **112**, C11007, https://doi.org/10.1029/2006JC003798.

Baldwin, M. P., and T. J. Dunkerton, 2001: Stratospheric harbingers of anomalous weather regimes. *Science*, **294**, 581–584, https://doi.org/10.1126/science.1063315.

——, and Coauthors, 2001: The quasi-biennial oscillation. *Rev. Geophys.*, **39**, 179–229, https://doi.org/10.1029/1999RG000073.

——, T. Hirroka, A. O'Neill, and S. Yoden, 2003: Major stratospheric warming in the SH in 2002. *SPARC Newsletter*, No. 20, SPARC International Project Office, Oberpfaffenhofen, Germany, 24–26, www.sparc-climate.org/wp-content/uploads/sites/5/2017/12/SPARCnewsletter_No20_Jan2003_redFile.pdf.

Bett, P. E., K. E. Williams, C. Burton, A. A. Scaife, A. J. Wiltshire, and R. Gilham, 2020: Skillful seasonal prediction of key carbon cycle components: NPP and fire risk. *Environ. Res. Commun.*, **2**, 055002, https://doi.org/10.1088/2515-7620/ab8b29.

Birner, T., and J. R. Albers, 2017: Sudden stratospheric warmings and anomalous upward wave activity flux. *SOLA*, **13A**, 8–12, https://doi.org/10.2151/sola.13A-002.

Butler, A. H., D. J. Seidel, S. C. Hardiman, N. Butchart, T. Birner, and A. Match, 2015: Defining sudden stratospheric warmings. *Bull. Amer. Meteor. Soc.*, **96**, 1913–1928, https://doi.org/10.1175/BAMS-D-13-00173.1.

Byrne, N. J., and T. G. Shepherd, 2018: Seasonal persistence of circulation anomalies in the Southern Hemisphere stratosphere and its implications for the troposphere. *J. Climate*, **31**, 3467–3483, https://doi.org/10.1175/JCLI-D-17-0557.1.

——, T. G. Shepherd, and I. Polichtchouk, 2019: Subseasonal-to-seasonal predictability of the Southern Hemisphere eddy-driven jet during austral spring and early summer. *J. Geophys. Res. Atmos.*, **124**, 6841–6855, https://doi.org/10.1029/2018JD030173.

Cai, W., P. van Rensch, T. Cowan, and H. H. Hendon, 2011: Teleconnection pathways of ENSO and the IOD and the mechanisms for impacts on Australian rainfall. *J. Climate*, **24**, 3910–3923, https://doi.org/10.1175/2011JCLI4129.1.

Ceppi, P., and D. L. Hartmann, 2013: On the speed of the eddy-driven jet and the width of the Hadley cell in the Southern Hemisphere. *J. Climate*, **26**, 3450–3465, https://doi.org/10.1175/JCLI-D-12-00414.1.

Charlton, A. J., and L. M. Polvani, 2007: A new look at stratospheric sudden warmings. Part I : Climatology and modeling benchmarks. *J. Climate*, **20**, 449–470, https://doi.org/10.1175/JCLI3996.1.

Domeisen, D. I., and Coauthors, 2020: The role of the stratosphere in subseasonal to seasonal prediction: 2. Predictability arising from stratosphere-troposphere coupling. *J. Geophys. Res. Atmos.*, **125**, e2019JD030923, https://doi.org/10.1029/2019JD030923.

Dowdy, A. J., 2018: Climatological variability of fire weather in Australia. *J. Appl. Meteor. Climatol.*, **57**, 221–234, https://doi.org/10.1175/JAMC-D-17-0167.1.

——, R. A. Vincent, D. J. Murphy, M. Tsutsumi, D. M. Riggin, and M. J. Jarvis, 2004: The large-scale dynamics of the mesosphere–lower thermosphere during the Southern Hemisphere stratospheric warming of 2002. *Geophys. Res. Lett.*, **31**, L14102, https://doi.org/10.1029/2004GL020282.

Esler, J. G., and R. K. Scott, 2005: Excitation of transient Rossby waves on the stratospheric polar vortex and the barotropic sudden warming. *J. Atmos. Sci.*, **62**, 3661–3682, https://doi.org/10.1175/JAS3557.1.

——, and N. J. Matthewman, 2011: Stratospheric sudden warmings as self-tuning resonances. Part II: Vortex displacement events. *J. Atmos. Sci.*, **68**, 2505–2523, https://doi.org/10.1175/JAS-D-11-08.1.

——, L. M. Polvani, and R. K. Scott, 2006: The Antarctic stratospheric sudden warming of 2002: A self-tuned resonance? *Geophys. Res. Lett.*, **33**, L12804, https://doi.org/10.1029/2006GL026034.

Eswaraiah, S., J. Kim, W. Lee, J. Hwang, K. N. Kumar, and Y. H. Kim, 2020: Unusual changes in the Antarctic middle atmosphere during the 2019 warming in the Southern Hemisphere. *Geophys. Res. Lett.*, **47**, e2020GL089199, https://doi.org/10.1029/2020GL089199.

Garreaud, R., 2018: Record-breaking climate anomalies lead to severe drought and environmental disruption in western Patagonia in 2016. *Climate Res.*, **74**, 217–229, https://doi.org/10.3354/cr01505.

Gillett, N. P., T. D. Kell, and P. D. Jones, 2006: Regional climate impacts of the Southern Annular Mode. *Geophys. Res. Lett.*, **33**, L23704, https://doi.org/10.1029/2006GL027721.

Gong, D., and S. Wang, 1999: Definition of Antarctic Oscillation index. *Geophys. Res. Lett.*, **26**, 459–462, https://doi.org/10.1029/1999GL900003.

Gray, L. J., M. J. Brown, J. Knight, M. Andrews, H. Lu, C. O'Reilly, and J. Anstey, 2020: Forecasting extreme stratospheric polar vortex events. *Nat. Commun.*, **11**, 4630, https://doi.org/10.1038/s41467-020-18299-7.

Harnik, N., R. K. Scott, and J. Perlwitz, 2005: Wave reflection and focusing prior to the major stratospheric warming of September 2002. *J. Atmos. Sci.*, **62**, 640–650, https://doi.org/10.1175/JAS-3327.1.

Hendon, H. H., E.-P. Lim, and H. Nguyen, 2014: Seasonal variations of subtropical precipitation associated with the southern annular mode. *J. Climate*, **27**, 3446–3460, https://doi.org/10.1175/JCLI-D-13-00550.1.

——, and Coauthors, 2019a: Rare forecasted climate event under way in the Southern Hemisphere. *Nature*, **573**, 495–495, https://doi.org/10.1038/d41586-019-02858-0.

——, A. B. Watkins, E.-P. Lim, and G. Young, 2019b: The air above Antarctica is suddenly getting warmer – Here's what it means for Australia. The Conversation, 8 September, https://theconversation.com/the-air-above-antarctica-is-suddenly-getting-warmer-heres-what-it-means-for-australia-123080.

——, E.-P. Lim, and S. Abhik, 2020: Impact of interannual ozone variations on the downward coupling of the 2002 Southern Hemisphere stratospheric warming. *J. Geophys. Res.*, **125**, e2020JD032952, https://doi.org/10.1029/2020JD032952.

Hio, Y., and S. Yoden, 2005: Interannual variations of the seasonal march in the Southern Hemisphere stratosphere for 1979–2002 and characterization of the unprecedented year 2002. *J. Atmos. Sci.*, **62**, 567–580, https://doi.org/10.1175/JAS-3333.1.

Holton, J. R., and H.-C. Tan, 1980: The influence of the equatorial quasi-biennial oscillation on the global circulation at 50 mb. *J. Atmos. Sci.*, **37**, 2200–2208, https://doi.org/10.1175/1520-0469(1980)037<2200:TIOTEQ>2.0.CO;2.

Hudson, D., and Coauthors, 2017: ACCESS-S1: The new Bureau of Meteorology multi-week to seasonal prediction system. *J. South. Hemisph. Earth Syst. Sci.*, **673**, 132–159, https://doi.org/10.22499/3.6703.001.

Hurrell, J. W., J. J. Hack, D. Shea, J. M. Caron, and J. Rosinski, 2008: A new sea surface temperature and sea ice boundary dataset for the community atmosphere model. *J. Climate*, **21**, 5145–5153, https://doi.org/10.1175/2008JCLI2292.1.

Hurwitz, M. M., P. A. Newman, L. D. Oman, and A. M. Molod, 2011: Response of the Antarctic stratosphere to two types of El Niño events. *J. Atmos. Sci.*, **68**, 812–822, https://doi.org/10.1175/2011JAS3606.1.

——, N. Calvo, C. I. Garfinkel, A. H. Butler, S. Ineson, C. Cagnazzo, E. Manzini, and C. Peña-Ortiz, 2014: Extra-tropical atmospheric response to ENSO in

the CMIP5 models. *Climate Dyn.*, **43**, 3367–3376, https://doi.org/10.1007/s00382-014-2110-z.

Johnson, S. J., and Coauthors, 2019: SEAS5: The new ECMWF seasonal forecast system. *Geosci. Model Dev.*, **12**, 1087–1117, https://doi.org/10.5194/gmd-12-1087-2019.

Jones, D. A., W. Wang, and R. Fawcett, 2009: High-quality spatial climate datasets for Australia. *Aust. Meteor. Oceanogr. J.*, **58**, 233–248, https://doi.org/10.22499/2.5804.003.

Jucker, M., 2016: Are sudden stratospheric warmings generic? Insights from an idealized GCM. *J. Atmos. Sci.*, **73**, 5061–5080, https://doi.org/10.1175/JAS-D-15-0353.1.

Kang, S. M., L. M. Polvani, J. C. Fyfe, and M. Sigmond, 2011: Impact of polar ozone depletion on subtropical precipitation. *Science*, **332**, 951–954, https://doi.org/10.1126/science.1202131.

Keeble, J., P. Braesicke, N. L. Abraham, H. K. Roscoe, and J. A. Pyle, 2014: The impact of polar stratospheric ozone loss on southern Hemisphere stratospheric circulation and climate. *Atmos. Chem. Phys.*, **14**, 13 705–13 717, https://doi.org/10.5194/acp-14-13705-2014.

Kidston, J., A. A. Scaife, S. C. Hardiman, D. M. Mitchell, N. Butchart, M. P. Baldwin, and L. J. Gray, 2015: Stratospheric influence on tropospheric jet streams, storm tracks and surface weather. *Nat. Geosci.*, **8**, 433–440, https://doi.org/10.1038/ngeo2424.

King, A. D., A. H. Butler, M. Jucker, N. O. Earl, I. Rudeva, 2019: Observed relationships between sudden stratospheric warmings and European climate extremes. *J. Geophys. Res. Atmos.*, **124**, 13 943–13 961, https://doi.org/10.1029/2019JD030480.

Kobayashi, S., and Coauthors, 2015: The JRA-55 Reanalysis: General specifications and basic characteristics. *J. Meteor. Soc. Japan. Ser. II*, **93**, 5–48, https://doi.org/10.2151/jmsj.2015-001.

Kodera, K., and Y. Kuroda, 2002: Dynamical response to the solar cycle. *J. Geophys. Res.*, **107**, 4749, https://doi.org/10.1029/2002JD002224.

Kuroda, Y., and K. Kodera, 1998: Interannual variability in the troposphere and stratosphere of the Southern Hemisphere winter. *J. Geophys. Res.*, **103**, 13 787–13 799, https://doi.org/10.1029/98JD01042.

Lawrence, Z. D., and G. L. Manney, 2020: Does the Arctic stratospheric polar vortex exhibit signs of preconditioning prior to sudden stratospheric warmings? *J. Atmos. Sci.*, **77**, 611–632, https://doi.org/10.1175/JAS-D-19-0168.1.

Lim, E.-P., H. H. Hendon, and D. W. J. Thompson, 2018: Seasonal evolution of stratosphere-troposphere coupling in the Southern Hemisphere and implications for the predictability of surface climate. *J. Geophys. Res. Atmos.*, **123**, 12 002–12 016, https://doi.org/10.1029/2018JD029321.

——, ——, G. Boschat, D. Hudson, D. W. J. Thompson, A. J. Dowdy, and J. M. Arblaster, 2019: Australian hot and dry extremes induced by weakenings of the stratospheric polar vortex. *Nat. Geosci.*, **12**, 896–901, https://doi.org/10.1038/s41561-019-0456-x.

——, and Coauthors, 2020: The 2019 Antarctic sudden stratospheric warming. *SPARC Newsletter*, No. 54, SPARC International Project Office, Oberpfaffenhofen, Germany, 10–13, www.sparc-climate.org/wp-content/uploads/sites/5/2017/12/SPARCnewsletter_Jan2020_WEB.pdf.

MacLachlan, C., and Coauthors, 2015: Global Seasonal Forecast System version 5 (GloSea5): A high-resolution seasonal forecast system. *Quart. J. Roy. Meteor. Soc.*, **141**, 1072–1084, https://doi.org/10.1002/qj.2396.

Marshall, G. J., 2003: Trends in the southern annular mode from observations and reanalyses. *J. Climate*, **16**, 4134–4143, https://doi.org/10.1175/1520-0442(2003)016<4134:TITSAM>2.0.CO;2.

Matsuno, T., 1970: Vertical propagation of stationary planetary waves in the winter Northern Hemisphere. *J. Atmos. Sci.*, **27**, 871–883, https://doi.org/10.1175/1520-0469(1970)027<0871:VPOSPW>2.0.CO;2.

McIntyre, M. E., and T. N. Palmer, 1983: Breaking planetary waves in the stratosphere. *Nature*, **305**, 593–600, https://doi.org/10.1038/305593a0.

Milinevsky, G., O. Evtushevsky, A. Klekociuk, Y. Wang, A. Grytsai, V. Shulga, and O. Ivaniha, 2020: Early indications of anomalous behaviour in the 2019 spring ozone hole over Antarctica. *Int. J. Remote Sens.*, **41**, 7530–7540, https://doi.org/10.1080/2150704X.2020.1763497.

Molod, A., and Coauthors, 2020: GEOS-S2S version 2: The GMAO high-resolution coupled model and assimilation system for seasonal prediction. *J. Geophys. Res. Atmos.*, **125**, e2019JD031767, https://doi.org/10.1029/2019JD031767.

Newman, P., and E. Nash, 2005: The unusual Southern Hemisphere stratosphere winter of 2002. *J. Atmos. Sci.*, **62**, 614–628, https://doi.org/10.1175/JAS-3323.1.

——, ——, and J. E. Rosenfield, 2001: What controls the temperature of the Arctic stratosphere during the spring? *J. Geophys. Res.*, **106**, 19 999–20 010, https://doi.org/10.1029/2000JD000061.

Nishii, K., and H. Nakamura, 2004: Tropospheric influence on the diminished Antarctic ozone hole in September 2002. *Geophys. Res. Lett.*, **31**, L16103, https://doi.org/10.1029/2004GL019532.

Noguchi, S., Y. Kuroda, K. Kodera, and S. Watanabe, 2020: Robust enhancement of tropical convective activity by the 2019 Antarctic sudden stratospheric warming. *Geophys. Res. Lett.*, **47**, e2020GL088743, https://doi.org/10.1029/2020GL088743.

Panofsky, H. A., and G. W. Brier, 1963: *Some Applications of Statistics to Meteorology*. Pennsylvania State University, 224 pp.

Peixoto, J. P., and A. H. Oort, 1992: *Physics of Climate*. 1st ed. AIP Press, 520 pp.

Phillips, N., and B. Nogrady, 2020: The race to decipher how climate change influenced Australia's record fires. *Nature*, **577**, 610–612, https://doi.org/10.1038/d41586-020-00173-7.

Randel, W. J., F. Wu, and R. S. Stolarski, 2002: Changes in column ozone correlated with the stratospheric EP flux. *J. Meteor. Soc. Japan*, **80**, 849–862, https://doi.org/10.2151/jmsj.80.849.

Rao, J., C. I. Garfinkel, I. P. White, and C. Schwartz, 2020: The Southern Hemisphere minor sudden stratospheric warming in September 2019 and its predictions in S2S models. *J. Geophys. Res. Atmos.*, **125**, e2020JD032723, https://doi.org/10.1029/2020JD032723.

Reisinger, A., R. L. Kitching, F. Chiew, L. Hughes, P. C. D. Newton, S. S. Schuster, A. Tait, and P. H. Whetton, 2014: Australasia. *Climate Change 2014: Impacts, Adaptation, and Vulnerability. Part B: Regional Aspects*, Cambridge University Press, 1371–1438, www.ipcc.ch/report/ar5/wg2/australasia/.

Reynolds, R. W., N. A. Rayner, T. M. Smith, D. C. Stokes, and W. Wang, 2002: An improved in situ and satellite SST analysis for climate. *J. Climate*, **15**, 1609–1625, https://doi.org/10.1175/1520-0442(2002)015<1609:AIISAS>2.0.CO;2.

Saji, N. H., and T. Yamagata, 2003: Possible impacts of Indian Ocean dipole mode events on global climate. *Climate Res.*, **25**, 151–169, https://doi.org/10.3354/cr025151.

——, B. N. Goswami, P. N. Vinayachandran, and T. Yamagata, 1999: A dipole mode in the tropical Indian Ocean. *Nature*, **401**, 360–363, https://doi.org/10.1038/43854.

Salby, M., P. Callaghan, and M. Guirlet, 2002: Interannual changes of temperature and ozone : Relationship between the lower and upper stratosphere. *J. Geophys. Res.*, **107**, 4342, https://doi.org/10.1029/2001JD000421.

Scaife, A. A., D. R. Jackson, R. Swinbank, N. Butchart, H. E. Thornton, M. Keil, and L. Henderson, 2005: Stratospheric vacillations and the major warming over Antarctica in 2002. *J. Atmos. Sci.*, **62**, 629–639, https://doi.org/10.1175/JAS-3334.1.

Scott, R. K., and L. M. Polvani, 2004: Stratospheric control of upward wave flux near the tropopause. *Geophys. Res. Lett.*, **31**, L02115, https://doi.org/10.1029/2003GL017965.

Seviour, W. J. M., S. C. Hardiman, L. J. Gray, N. Butchart, C. MacLachlan, and A. A. Scaife, 2014: Skillful seasonal prediction of the southern annular mode and Antarctic ozone. *J. Climate*, **27**, 7462–7474, https://doi.org/10.1175/JCLI-D-14-00264.1.

Shen, X., L. Wang, and S. Osprey, 2020: Tropospheric forcing of the 2019 Antarctic sudden stratospheric warming. *Geophys. Res. Lett.*, **47**, e2020GL089343, https://doi.org/10.1029/2020GL089343.

Shepherd, T. G., 2019: Storyline approach to the construction of regional climate change information. *Proc. Roy. Soc.*, **475A**, 20190013, https://doi.org/10.1098/rspa.2019.0013.

——, R. A. Plumb, and S. C. Wofsy, 2005: PREFACE. *J. Atmos. Sci.*, **62**, 565–566, https://doi.org/10.1175/JAS-9999.1.

Shiotani, M., N. Shimoda, and I. Hirota, 1993: Interannual variability of the stratospheric circulation in the Southern Hemisphere. *Quart. J. Roy. Meteor. Soc.*, **119**, 531–546, https://doi.org/10.1002/qj.49711951110.

Sjoberg, J. P., and T. Birner, 2014: Stratospheric wave-mean flow feedbacks and sudden stratospheric warmings in a simple model forced by upward wave activity flux. *J. Atmos. Sci.*, **71**, 4055–4071, https://doi.org/10.1175/JAS-D-14-0113.1.

Stolarski, R. S., R. D. McPeters, and P. Newman, 2005: The ozone hole of 2002 as measured by TOMS. *J. Atmos. Sci.*, **62**, 716–720, https://doi.org/10.1175/JAS-3338.1.

Taguchi, M., and S. Yoden, 2002: Internal interannual variability of the troposphere–stratosphere coupled system in a simple global circulation model. Part I: Parameter sweep experiment. *J. Atmos. Sci.*, **59**, 3021–3036, https://doi.org/10.1175/1520-0469(2002)059<3021:IIVOTT>2.0.CO;2.

Takaya, Y., and Coauthors, 2018: Japan Meteorological Agency/Meteorological Research Institute-Coupled Prediction System version 2 (JMA/MRI-CPS2): Atmosphere–land–ocean–sea ice coupled prediction system for operational seasonal forecasting. *Climate Dyn.*, **50**, 751–765, https://doi.org/10.1007/s00382-017-3638-5.

Thompson, D. W. J., and J. M. Wallace, 2000: Annular mode in the extratropical circulation. Part I : Month-to-month variability. *J. Climate*, **13**, 1000–1016, https://doi.org/10.1175/1520-0442(2000)013<1000:AMITEC>2.0.CO;2.

——, M. P. Baldwin, and S. Solomon, 2005: Stratosphere–troposphere coupling in the Southern Hemisphere. *J. Atmos. Sci.*, **62**, 708–715, https://doi.org/10.1175/JAS-3321.1.

Wang, G., and H. H. Hendon, 2007: Sensitivity of Australian rainfall to inter–El Niño variations. *J. Climate*, **20**, 4211–4226, https://doi.org/10.1175/JCLI4228.1.

Wargan, K., B. Weir, G. L. Manney, S. E. Cohn, and N. J. Livesey, 2020: The anomalous 2019 Antarctic ozone hole in the GEOS constituent data assimilation system with MLS observations. *J. Geophys. Res. Atmos.*, **125**, e2020JD033335, https://doi.org/10.1029/2020JD033335.

Wilks, D. S., 2006: *Statistical Methods in the Atmospheric Sciences*. 2nd ed. Academic Press, 592 pp.

Yamazaki, Y., and Coauthors, 2020: September 2019 Antarctic sudden stratospheric warming: quasi-6-day wave burst and ionospheric effects. *Geophys. Res. Lett.*, **47**, e2019GL086577, https://doi.org/10.1029/2019GL086577.